SCIEPublish

Review

Engineering of Cu-Based Quaternary Sulfide Nanomaterials for Photocatalytic Applications

Bingqian Zu, Song Chen, Qiren Jin and Liang Wu *

Key Laboratory of Functional Molecular Solids, Ministry of Education, School of Chemistry and Materials Science, Anhui Normal University, Wuhu 241002, China; zubingqian@ahnu.edu.cn (B.Z.); chensong@ahnu.edu.cn (S.C.); 2321011421@ahnu.edu.cn (Q.J.)

* Corresponding author. E-mail: wuliang@ahnu.edu.cn (L.W.)

Received: 14 June 2024; Accepted: 15 October 2024; Available online: 22 October 2024

ABSTRACT: Semiconductor nanomaterials have been widely used as light-responsive photocatalysts for solar-to-fuel conversion over the past decade. However, the wide band gap of the most reported photocatalysts stems from light absorption in the visible region and results in low solar conversion efficiency. Therefore, it is necessary to develop new semiconductor nanomaterials with high absorption coefficients over the visible region as photocatalysts. The most promising candidates include Cu-based quaternary sulfide nanomaterials (CQSNs), such as Cu-II-III-S (e.g., CuZnInS, CuZnGaS), Cu-II-IV-S (e.g., Cu_2ZnSnS_4, Cu_2ZnGeS_4), and I-III-IV-S (e.g., $CuInSnS_4$, Cu_3GaSnS_5). This review provides a comprehensive overview of the recent progress in developing CQSNs for various photocatalytic applications. Firstly, we present an overview of the synthesis of CQSNs with precise control over crystal phase, composition, size, and shape using solution-based methods. Then, the enhancement of photocatalytic performance was presented via the engineering of CQSNs, which included surface engineering, elemental doping, cocatalyst loading, vacancy engineering, and interface engineering. Subsequently, we further introduce the photocatalytic applications in the fields of photocatalytic and photoelectrochemical hydrogen conversion, CO_2 reduction, organic synthesis, and pollutant degradation. Lastly, this review ends with views on the current challenges and opportunities of CQSNs in future studies.

Keywords: Cu-based quaternary sulfide nanomaterials; Photocatalytic hydrogen conversion; Photoelectrochemical hydrogen production; Photocatalytic CO_2 reduction; Photocatalytic organic synthesis; Photocatalytic pollutant removal

1. Introduction

The majority of the utilized energy is accompanied by CO_2 emissions, resulting in well-established greenhouse effects and numerous significant environmental concerns [1]. The global CO_2 emission must be limited to approximately 500 billion tonnes in order to effectively control the rise in global temperature to 1.5 °C [2]. In September 2020, China explicitly proposed the targets of achieving a "carbon peak" by 2030 and a "carbon neutrality" by 2060. To advance the implementation of the "dual carbon strategy" and mitigate carbon emissions, it primarily encompasses the following three aspects: (I) enhancing energy conservation on the demand side and optimizing energy utilization efficiency, (II) adjusting the energy mix and vigorously promoting low-carbon energy sources on the supply side, (III) concurrently advancing carbon sink development and carbon capture. The annual global CO_2 emissions amount to approximately 40 billion tonnes, with around 85% originating from the utilization of fossil fuels [3]. Therefore, there is an urgent need to explore clean, renewable, and carbon-neutral energy resources as substitutes for fossil fuels. Solar energy, the most abundant and environmentally friendly power source, holds great promise as a viable alternative that can play an indispensable role in all three aspects mentioned above. It will provide substantial support towards achieving the "double carbon" goal.

Solar-driven photocatalysis technology holds significant potential for addressing environmental issues and energy shortages [4–9]. For example, converting solar energy to hydrogen provides an efficient approach to green hydrogen production. At the same time, photocatalytic CO_2 reduction serves as a valuable method for carbon capture and the generation of high-value-added products [10–13]. The photocatalytic reaction can be divided into three steps: (I) The

https://doi.org/10.70322/prp.2024.10009

photocatalysts absorb sunlight to generate carriers (excited electrons and holes); (II) The photogenerated carriers migrate to the surface of the photocatalysts; (III) The photogenerated carriers participate in the redox reaction [14,15]. The efficiency of photocatalytic conversion can be optimized by enhancing three key thermodynamic and dynamic parameters: light absorption efficiency, charge separation efficiency, and redox reaction efficiency [16,17]. The excitation of electrons to the conduction band (CB) of semiconductor photocatalysts occurs under solar light irradiation while simultaneously leaving holes in the valence band (VB) [18–20]. Since the groundbreaking discovery by Prof. Akira Fujishima and Prof. Kenichi Honda in 1972 [21], which reported the successful photocatalytic hydrogen production over a TiO_2 photocatalyst, there has been an increasing focus on the development of semiconductor photocatalysts, leading to remarkable achievements [22–26]. The rapid development of nanotechnology has strongly promoted the design and synthesis of nanostructured semiconductor photocatalysts. Compared to bulk semiconductor materials, nanostructured semiconductor photocatalysts offer distinct advantages due to their unique physical and chemical properties, which arise from quantum effects and a greatly increased surface area [27–29].

A series of semiconductors have been explored as photocatalysts, such as metal nitrides, metal oxides, metal oxysulfides, metal sulfides, and polymers [30–34]. However, most of the reported semiconductor photocatalysts exhibit limited sunlight absorption capability, thereby significantly constraining their potential for photocatalytic applications. The development of a nanostructured photocatalyst with a high absorption coefficient across the entire visible range is essential for achieving efficient photocatalytic reactions. Cu-based quaternary sulfide (CQS) compounds can be regarded as derivatives of ZnS/CdS by substituting Zn/Cd with environmentally friendly elements. These compounds exhibit exceptional properties in terms of visible light absorption and possess suitable energy band structures for efficient sunlight absorption, making them promising candidates for potential photocatalysts [35–38]. In addition, the energy band structure of CQSs can be easily regulated to optimize their visible light absorption capacity [39,40]. In recent years, the synthesis and photocatalytic applications of Cu-based quaternary sulfide nanomaterials (CQSNs) have garnered significant attention.

In this review, we provide a summary of recent research on CQSNs—particularly those that belong to the Cu-II-III-S (e.g., CuZnInS, CuZnGaS), Cu-II-IV-S (e.g., Cu_2ZnSnS_4, Cu_2ZnGeS_4), and I-III-IV-S (e.g., $CuInSnS_4$, Cu_3GaSnS_5) semiconductor families—as promising visible-light-driven photocatalysts (Figure 1). We initially present a concise overview of the solution synthesis method for fabricating CQSNs with varying compositions, shapes, sizes, and crystal phases, which have significantly impacted the photocatalytic performances of semiconductor materials. Then, the photocatalytic property of CQSNs can be considerably improved through strategies that modify the semiconductor band structure, facilitate efficient charge separation, and improve the efficiency of redox reactions. These strategies include surface engineering, elemental doping, cocatalyst loading, vacancy and interface engineering. We then present various photocatalytic applications of these CQSNs, focusing on solar-to-hydrogen conversion, CO_2 reduction, photoelectrochemical hydrogen production, organic synthesis, and pollutant removal. Finally, we also discuss the challenges and opportunities for future studies involving CQSNs.

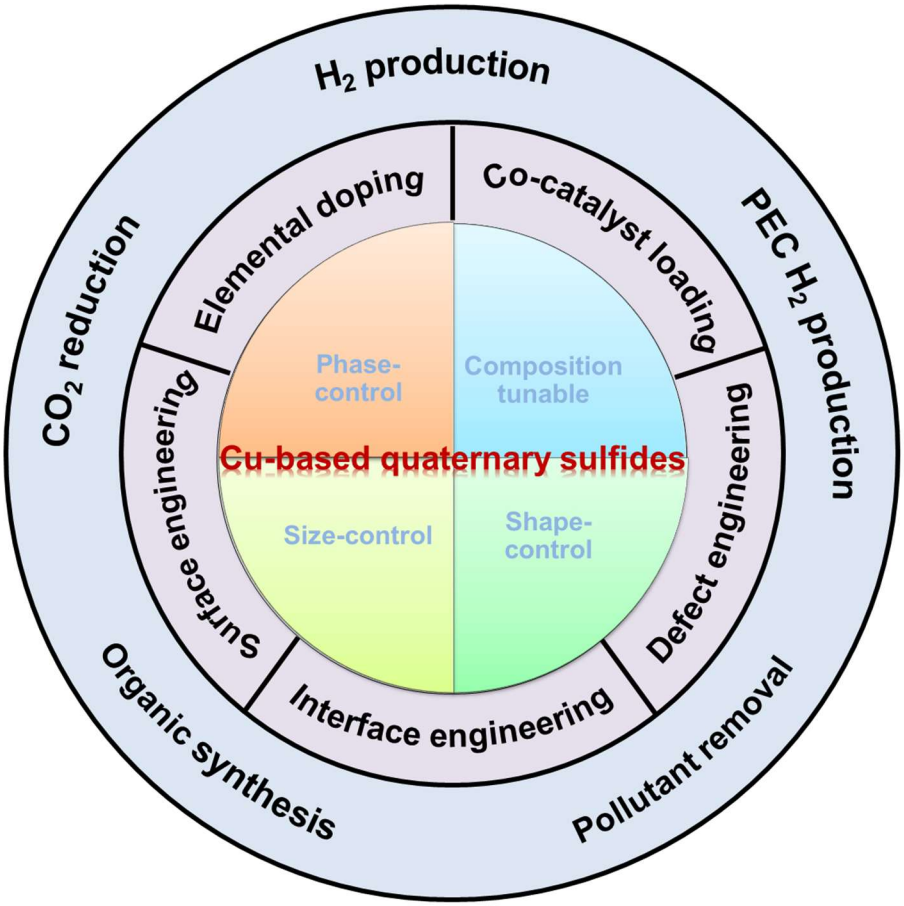

Figure 1. Schematic illustration of the control synthesis, engineering, and photocatalytic applications of Cu-based quaternary sulfide nanomaterials.

2. Controlled Synthesis of Cu-Based Quaternary Sulfide Nanomaterials

Bulk CQS semiconductors can easily be obtained throuhigh-temperature solid-state methods [41,42]. In contrast, CQSNs are typically synthesized at relatively lower temperatures using solution-based approaches, such as colloidal chemical synthesis and hydrothermal/solvothermal methods [43,44]. The significant advancements in solution-based synthesis of nanomaterials have facilitated precise control over composition, shape, size, and crystal phase—all crucial factors influencing the photocatalytic activity of CQSNs. This section provides a summary of studies on the controlled synthesis of CQSNs.

2.1. Composition-Tunable Synthesis

The band structure of CQSNs can be easily regulated to enhance their photocatalytic properties by adjusting the element composition [45–47]. The optical and electronic properties of copper-based quaternary chalcogenides, such as band structure, photogenerated charge carrier separation, and transfer, are significantly influenced by the ratio of Zn [48–50]. Tang and coauthors have developed a colloidal method for synthesizing one-dimensional (1D) Cu-Zn-Ga-S (CZGS) nanorods with varying Zn contents and investigated their photocatalytic hydrogen production properties [51]. As shown in Figure 2a, the synthesized CZGS nanorods have a wurtzite (WZ) crystal structure, which remains unaffected by the Ga:Zn feeding molar ratio. The incorporation of Zn facilitated the growth of quaternary Cu−Ga−Zn−S nanorods along the [0001] direction. It promoted the formation of elongated nanostructures while preserving their 1D-shaped morphology and wurtzite crystal phase. As a result, the presence of Zn cations increases the length of the obtained nanorods (Figure 2b–f). Figure 2g shows a high-resolution transmission electron microscopy (HRTEM) image of CZGS nanorods with a Ga:Zn feeding molar ratio of 7:1. There are two series of vertical lattice fringes with spacings of 3.09 and 3.29 Å, corresponding to the (0002) and (10-10) planes of WZ CZGS. The alteration of optical properties in CZGS nanorods induced by composition was further characterized via absorption spectroscopy. The absorption band edge exhibits a noticeable blue shift (Figure 2h), while the bandgap increases (Figure 2i) with an increasing Ga:Zn feeding molar ratio, respectively. The photocatalytic hydrogen production performances of CZGS nanorods can be

effectively regulated by adjusting the Ga:Zn feeding molar ratio. The CZGS nanorods with a Ga:Zn feeding molar ratio of 7:1 exhibit the best photocatalytic performances with a hydrogen evolution rate of 2.101 mmol h^{-1} g^{-1} (Figure 2j).

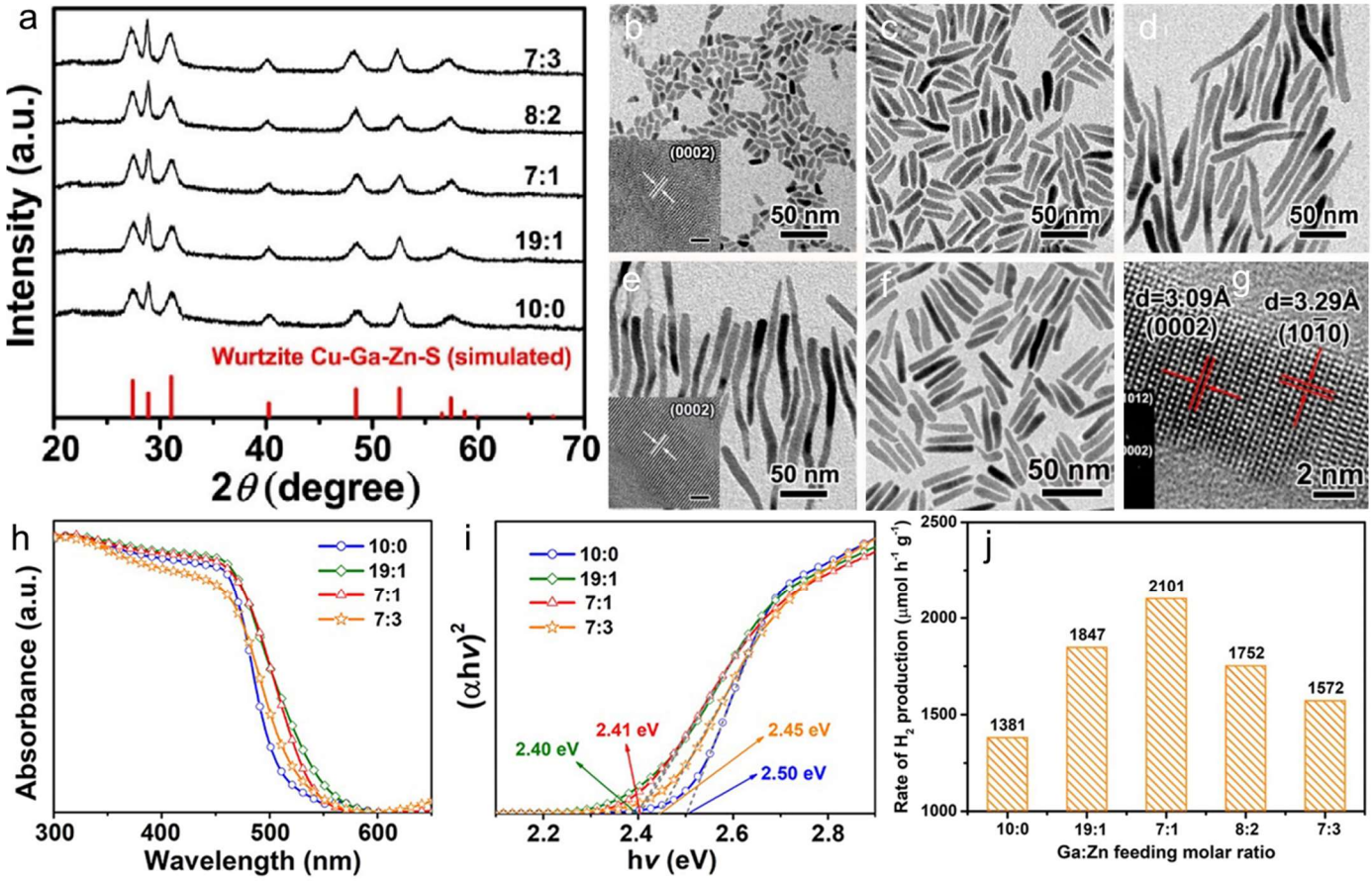

Figure 2. (**a**–**f**) X-ray diffraction (XRD) patterns and TEM images of CZGS NRs synthesized with Ga:Zn feeding molar ratios of 10:0, 19:1, 8:2, 7:3, and 7:1. (**g**) HRTEM image of CZGS NRs synthesized with Ga:Zn molar ratios of 7:1. (**h**,**i**) Diffuse reflectance spectroscopy spectra and the corresponding Tauc plots of CZGS nanorods. (**j**) Photocatalytic hydrogen production rates of the synthesized CZGS nanorods [51].

The CQS compounds can be regarded as alloys composed of binary sulfides and ternary sulfides, allowing for the adjustment of their composition by manipulating the ratio between these two types of sulfides [52–54]. For example, Cu-Zn-In-S (CZIS)—a solid solution that is created by alloying with binary ZnS (ZS) and ternary $CuInS_2$ (CIS)—shows a ZS:CIS molar ratio-dependent absorption and photocatalytic performance. The bandgap of ZS is too wide for efficient visible-light utilization, whereas CIS has a suitable conduction band minimum to facilitate the reduction of H_2O to H_2. The alloying of ZS and CIS can eliminate these drawbacks and optimize the photocatalytic properties of CZIS nanocrystals. A series of alloyed CZIS nanostructures have been developed for photocatalytic applications, such as zero-dimensional (0D) zinc-blende (ZB) CZIS quantum dots, 1D WZ CZIS nanorods, two-dimensional (2D) WZ CZIS nanobelts and three-dimensional (3D) ZB nanostructures [55–58]. The photocatalytic hydrogen production performance of all CZIS nanostructures depends on the molar ratio of ZS:CIS.

2.2. Shape-Controlled Synthesis

Refining the shape of nanostructures can enhance their functional capabilities, making them more suitable for advanced applications [59–61]. The synthesis of CQSNs with tailored morphology is crucial for their photocatalytic applications, as different shapes confer diverse physical and chemical properties [62]. Taking Cu_2ZnSnS_4 (CZTS) for an instant, WZ CZTS with different shapes can be achieved by selecting suitable synthesis methods. Cabot and coauthors reported a scalable colloidal method for the high-yield production of 0D CZTS nanocrystals [63]. As shown in Figure 3a, the obtained monodisperse CZTS nanocrystals exhibit a quasi-spherical shape with minimal size dispersion (below 10%). This can be attributed to the efficient mixing and heat transfer within the reaction solution and precise control of heating ramp stability achieved through intensive argon bubbling. The HRTEM image and the fast Fourier transform (FFT) pattern show that the CZTS nanocrystals have a WZ phase (Figure 3b). Ryan and coauthors have

successfully prepared 1D WZ stoichiometric CZTS nanorods using 1-dodecanethiol (1-DDT) and tert-dodecyl mercaptan (t-DDT) as sulfur sources [64]. The obtained CZTS nanorods have an average diameter of 11 ± 0.5 nm and a length of 35 ± 3 nm (Figure 3c). The HRTEM image of an individual nanorod exhibited a lattice fringe with an interplanar spacing of 0.32 nm, corresponding to the (0002) plane of WZ CZTS (Figure 3d), clarifying the WZ phase of the obtained nanorods.

2D nanostructures (e.g., nanoplates and nanosheets) exhibit great potential as light-responsive photocatalysts due to their extensive surface area and exposed special facets [65–67]. Bao and coauthors synthesized WZ CZTS nanosheets using a one-pot thermal decomposition method using 1-DDT as both the reaction solvent and sulfur source [68]. The obtained thin CZTS nanosheets exhibited predominantly quasi-triangular and hexagonal morphologies, with an average size ranging from 300 to 400 nm (Figure 3e). The HRTEM image revealed lattice fringes exhibiting an interplanar spacing of 0.33 nm, corresponding to the (100) family planes of WZ CZTS (Figure 3f). The selected area electron diffraction (SAED) pattern (inset of Figure 3f), combined with the HRTEM image, indicates that the WZ CZTS nanosheets expose the high-energy (002) plane and exhibit a well-crystallized, single-crystalline nature. 3D nanostructures have also been synthesized to improve the photocatalytic activity of semiconductor photocatalysts, as these nanoscale assemblies can serve as active sites for photocatalytic reactions [69–71]. Xu and coauthors used a top-down synthetic strategy to prepare 3D WZ CZTS nanoboxes [72]. The CZTS nanoboxes were produced via reacting Cu_2O nanocubes with Zn^{2+} ions and tin metal chalcogenide complexes at pH = 7 (Figure 3g). The interplanar spacings of 0.33 nm shown in Figure 3f correspond to the (010) and (100) planes of WZ CZTS, illustrating the WZ structure of the synthesized nanoboxes.

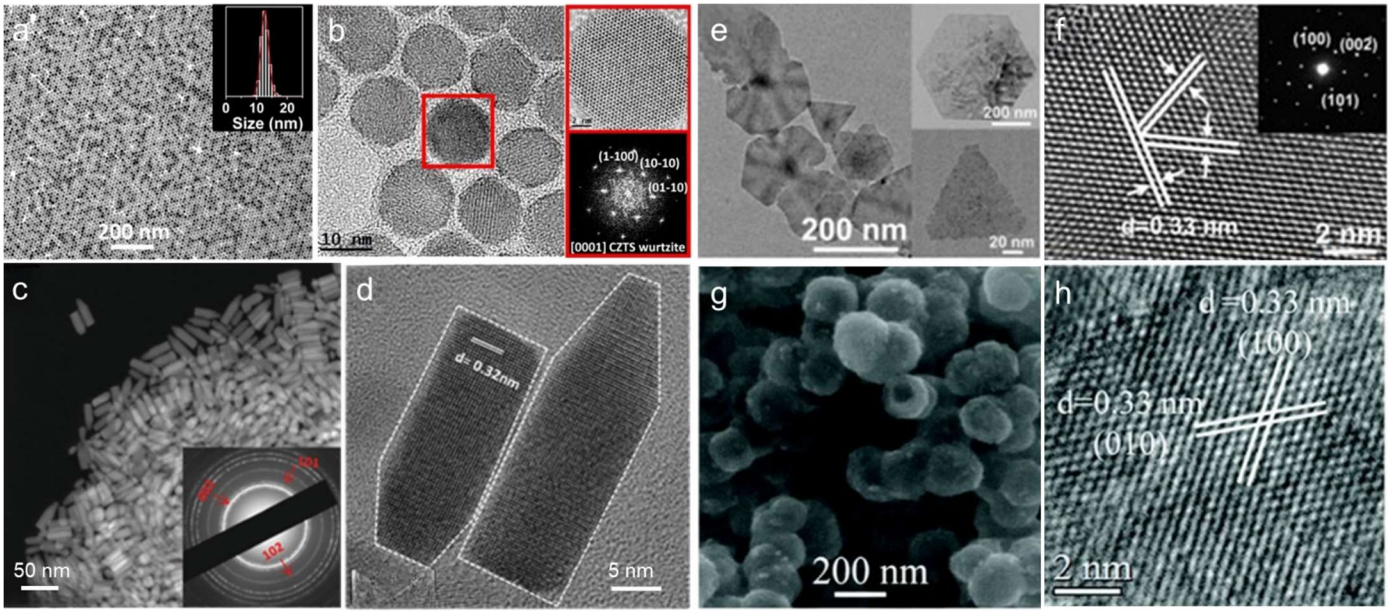

Figure 3. TEM and HRTEM images of WZ CZTS (**a**,**b**) nanocrystals [63], (**c**,**d**) nanorods [64], (**e**,**f**) nanosheets [68], and (**g**,**h**) nanoboxes [72]. The insert in (**a**) is the graph of size distribution. The inserts in (**b**) are the HRTEM image of the selected nanocrystals and the corresponding FFT pattern. The inserts in (**c**,**f**) are the SAED patterns.

2.3. Size-Controlled Synthesis

The size of a semiconductor photocatalyst is a key factor in modifying its photocatalytic performances as it directly affects the surface area, which determines the number of available surface-active reaction sites for photocatalytic [73–75]. Otherwise, size can be used to regulate the dynamics of electron-hole recombination. In general, reducing the size of a semiconductor photocatalyst enhances its photocatalytic performance by decreasing bulk charge recombination and increasing the availability of surface-active sites [76,77]. When nanomaterials are too small, the strong quantum confinement widens the band gap, thereby limiting their absorption range to visible light [78,79]. Moreover, surface carrier recombination becomes significant and can overshadow the benefits of a large surface area. Therefore, it is necessary to synthesize photocatalysts in various sizes to determine the optimum size for achieving maximum photocatalytic properties. The manipulation of reaction conditions such as solvent and ligand quantities, reaction time, and temperature allows for facile preparation of nanocrystals with different sizes.

Xie and coauthors have successfully synthesized CZIS nanocrystals, achieving size control through temperature-dependent reaction [80]. The size of the CZIS nanocrystals increased from 3.0 to 7.0 nm as the reaction temperature

was raised from 180 to 240 °C. Torimoto and coauthors successfully achieved the controlled synthesis of CZTS nanocrystals by manipulating the amount of oleylamine (OLA) and adjusting the reaction temperature [81]. As shown in Figure 4a–d, CZTS nanoparticles with an average diameter of ca. 2.8 and ca. 3.5 nm are produced at 150 °C by adding 0.13 and 2.0 mmol of OLA, respectively. Figure 4e–h shows that the CZTS nanocrystals with an average diameter of ca. 2.9 and 5.2 nm are obtained at 120 and 180 °C by adding 0.5 mmol of OLA, respectively. The obtained CZTS nanoparticles displayed size-dependent PEC properties.

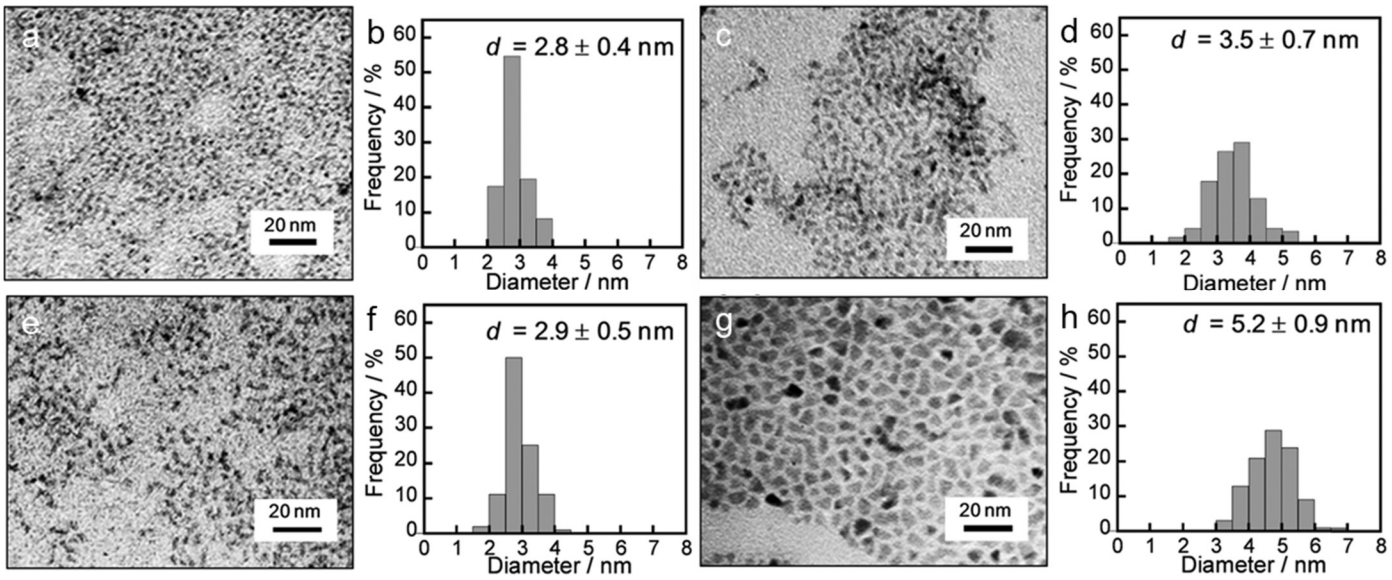

Figure 4. TEM images and size distribution graphs of the CZTS nanoparticles synthesized by the addition of (**a**,**b**) 0.13 mmol of OLA at 150 °C, (**c**,**d**) 2.0 mmol of OLA at 150 °C, (**e**,**f**) 0.5 mmol of OLA at 120 °C, (**g**,**h**) 0.5 mmol of OLA at 280 °C [81].

2.4. Phase-Controlled Synthesis

The crystal structure of semiconductor materials is an additional crucial factor that can impact their photocatalytic performance [82–84]. For example, the photocatalytic activity of anatase phase TiO2 nanocrystals is higher than that of the rutile phase [85]. CQSs are known to exist in two types of crystal phases: WZ and ZB [86]. ZB types derived from cubic ZB ZnS are classified into two structures: the cation-disordered cubic structure and the cation-ordered tetragonal structure (e.g., kesterite) [87]. Meanwhile, there are cation-disordered hexagonal structures and cation-ordered orthorhombic structures (e.g., WZ-kersterite, WZ-stannite) in WZ-type Cu-based quaternary sulfides [88]. The ZB phase is thermodynamically more stable than its WZ counterpart in the majority of situations and exhibits greater ease of synthesis.

In order to synthesize phase-pure products, it is necessary to carefully select reaction conditions that favor the crystalline of a specific crystal phase over another. It has been established that the choice of ligands/solvents plays a crucial role in determining the crystal phase in colloidal methods. Previous studies have shown that long-chain alkanethiols (e.g., 1-DDT), which not only act as an additional sulfur source but also function as surfactants, are advantageous for promoting the formation of the metastable WZ Cu-based multinary sulfide nanomaterials, such as CIS, Cu_2SnS_3, Cu_2CdGeS_4, and CZTS [89–92]. Lam and coauthors have successfully synthesized kersterite and WZ CZTS nanocrystals using element S (Figure 5a) and 1-DDT (Figure 5d) as sulfur sources, respectively [93]. The synthesized kesterite CZTS nanocrystals have an irregular morphology with an average size of 19.8 ± 6.5 nm (Figure 5b). The lattice fringes (Figure 5c) were found to be 0.27 and 0.33 nm, corresponding to the (020) planes and (11-1) planes for kesterite CZTS. The obtained WZ CZTS nanocrystals possess a nearly spherical shape with an average size of 12.9 ± 1.2 nm (Figure 5e). The HRTEM image (Figure 5f) displays lattice fringes with an interplanar spacing of 0.33 nm, corresponding to the (100) planes for WZ CZTS. In addition, phase-selective synthesis can also be accomplished by manipulating other experimental conditions, such as reaction temperature, templets, and precursors [94–96].

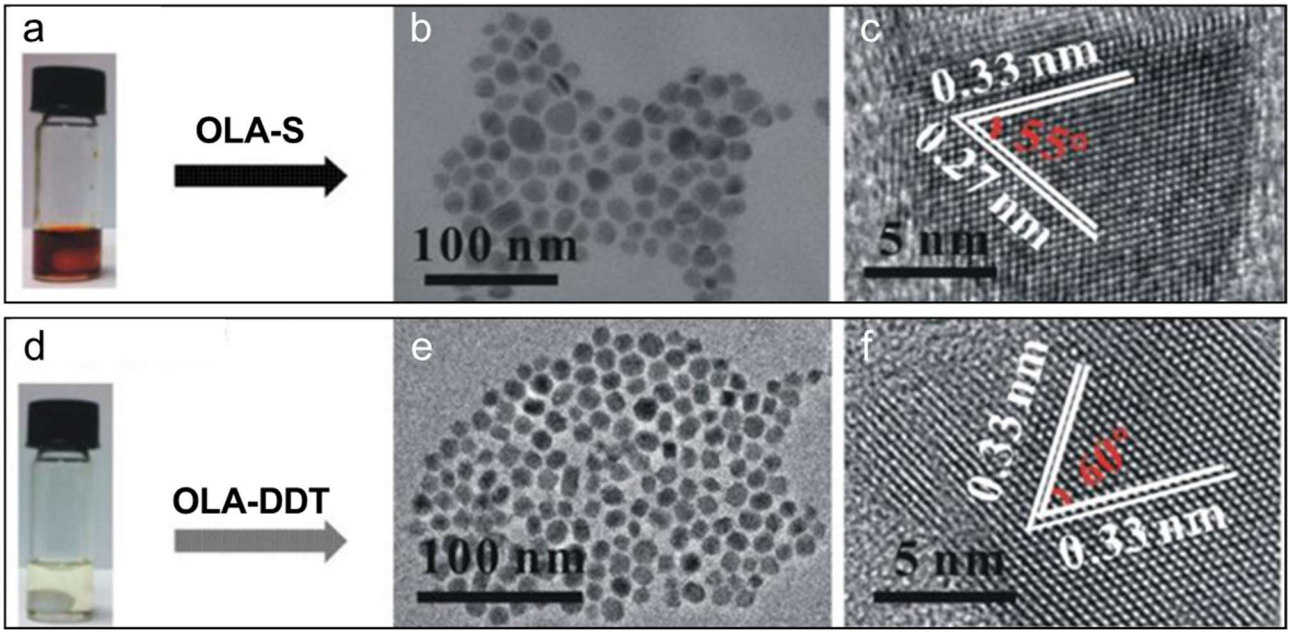

Figure 5. (**a**) Photo of OLA-S solution. (**b**,**c**) TEM and HRTEM images of CZTS nanoparticles synthesized using sulfur. (**d**) Photo of OLA-S solution. (**e**,**f**) TEM and HRTEM images of CZTS nanoparticles synthesized using 1-DDT [93].

3. Strategies for Photocatalytic Activity Improvement

The photocatalytic performance of pristine CQSNs is often limited by their poor light absorption capability, rapid recombination rate of electron-hole pairs, and sluggish reaction kinetics. As a new type of photocatalysts, the studies and applications of CQSN photocatalysts are comparatively limited compared to ZnS/CdS photocatalysts. At the same time, their photocatalytic activity is relatively low and requires further enhancement [24,28,72,76]. Therefore, various optimization strategies have been employed to enhance their photocatalytic performances. These modulation strategies are categorized into surface engineering, elemental doping, co-catalyst loading, defect management, and interface engineering.

3.1. Surface Engineering

Surface engineering, such as the regulation of surface crystal facets, facilitates the creation of uniform and abundant atomic-level sites for the photocatalytic reaction [97–99]. Different crystal facets in semiconductor photocatalysts typically exhibit varying levels of photocatalytic activity [100–102]. The manipulation of semiconductors to expose their most active facet represents an efficient approach to enhancing their photocatalytic performance [103–105]. In 2D materials, the exposure of more surface atoms enhances the adsorption of target molecules and provides additional reaction sites, which promotes catalytic reactions and results in reduced material thickness [106,107]. Furthermore, the shorter charge transfer distance significantly decreases the recombination probability of the electron-hole pairs, thereby enabling highly efficient carrier utilization. Therefore, engineering semiconductor photocatalysts to obtain ultrathin 2D structures that expose the most active crystal facets can effectively enhance the photocatalytic properties.

We have reported the surface engineering of single crystalline CZIS and CZGS nanobelts for achieving efficient solar-to-hydrogen production [57]. We first explored the relevant Gibbs free energy (ΔG_H) for hydrogen evolution reaction of (0001), (1010), and (1011) facets of WZ CZGS (Figure 6a) via density functional theory (DFT) calculation. As shown in Figure 6b, the ΔG_H of (0001) is the smallest, indicating that the (0001) facet had the smallest binding strength to atomic hydrogen. Following the Bell–Evans–Polanyi principle, the (0001) is the most active facet for photocatalytic hydrogen generation. Then, we designed a simple colloidal method assisted by OLA and DDT to synthesize a 2D single crystalline WZ CZIS with exposed (0001) facets and 2D single crystalline WZ CZIS. The obtained CZIS possesses a typical WZ structure (Figure 6c). As shown in Figure 6d, the obtained 2D CZIS presents a nanobelt morphology. The HRTEM images (Figure 6e,f) and SAED patterns (Figure g,h) of the randomly selected areas in Figure 6c indicate that the synthesized CZIS nanobelts possess a WZ structure, the single crystalline nature and a surface crystal facet of (0001). Moreover, the obtained CZIS nanobelts exhibited an excellent photocatalytic performance with a hydrogen evolution rate of 3.35 mmol h^{-1} $g^{-1,}$ which is higher than that of the nanoparticles and nanorods which exposed lesser (0001) facet (Figure 6i). Importantly, the CZIS and CZGS nanobelts display excellent

photocatalytic stability, as evidenced by the absence of any decrease in the rate of photocatalytic hydrogen production after six cycles (Figure 6j).

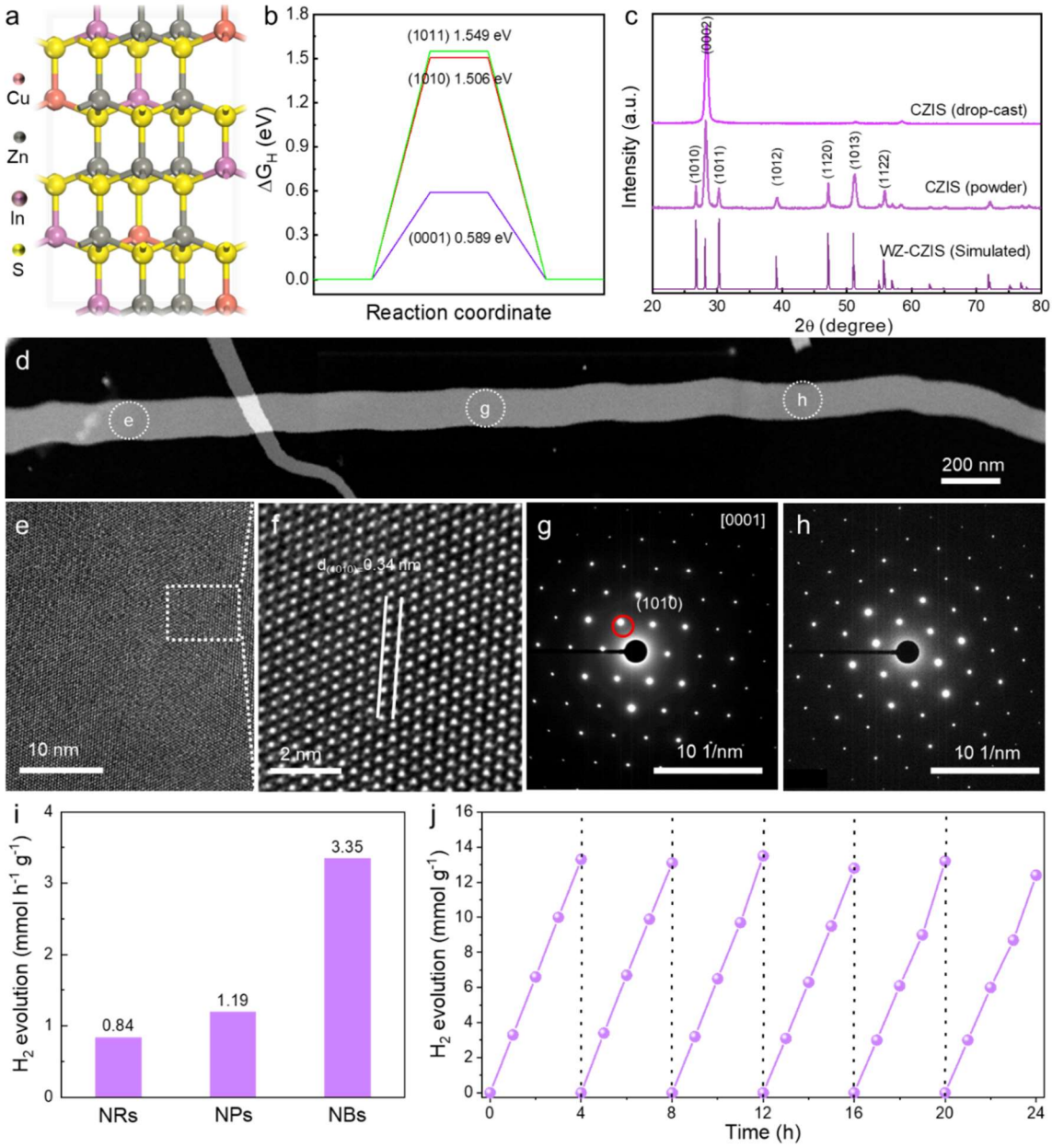

Figure 6. (**a**) Crystal model of WZ CZIS. (**b**) Reaction Gibbs energy diagram for H_2 evolution on different crystal facets of WZ CZIS. (**c**) XRD patterns of the obtained CZIS nanobelts. (**d**–**h**) HAADF-STEM image, HRTEM images, and SAED patterns of CZIS nanobelts. (**i**) Comparison of the photocatalytic hydrogen production properties of CZIS nanoparticles, nanorods, and nanobelts. (**j**) Recycle hydrogen generation property of CZIS nanobelt photocatalyst [57].

3.2. Elemental Doping

Regulating the electronic energy band structure is a fundamental approach for optimizing the photocatalytic performances of semiconductor photocatalysts. Incorporating heteroatoms into semiconductor materials is an effective strategy to modulate their physical and chemical properties, such as extending light absorption range, adjusting bandgap structure, providing active sites, improving electric conductivity, and facilitating the H adsorption and desorption process. This offers ample opportunities for fine-tuning their photocatalytic capabilities [20,108,109]. Till now, many metal atoms (e.g., Cu, Mo, Pt, Ni, Fe, etc.) have been utilized to modify the semiconductor materials to enhance their photocatalytic activity [24,110–113]. Metal heteroatoms can serve as trap sites to reduce carrier recombination and also facilitate the transfer of carriers to surface redox reaction sites, thereby enhancing photocatalytic performance. Zhan and coauthors incorporated Cu into $ZnIn_2S_4$ to optimize its photocatalytic properties and provided atomic-level insights into the role of Cu atoms in modifying $ZnIn_2S_4$ [114]. The doping of Cu atoms introduces electronic acceptor states in

close proximity to VB maximum, facilitating efficient carrier transport and increasing charge density, resulting in improved performance in photocatalytic hydrogen evolution. However, excessive doping leads to a significant upshift of VB maximum and distortion in atomic structure, leading to accelerated carrier recombination rates and, consequentially, a drastic reduction in photoactivity.

The previous reports indicate that non-metal dopants, such as C, O, and P elements, can easily substitute the exposed S atoms on the surface of sulfides to enhance their photocatalytic properties [115–117]. For example, Chen and coauthors prepared C-doped SnS_2 nanosheets as a photocatalyst for efficient solar fuel production [118]. The C-doped SnS_2 nanosheets show higher selectivity and activity for photocatalytic CO_2 conversion under visible light. We also have utilized the P atom to manipulate the carrier dynamics of single crystalline quaternary sulfide nanobelts [119]. The P-doped CZIS nanobelts were synthesized via annealing CZIS nanobelts with sodium hypophosphite monohydrate under an argon atmosphere (Figure 7a). As shown in Figure 2b, the P atom has been uniformly entered into the CZIS nanobelts. Importantly, the P-doped CZIS nanobelts inherited the crystal structure and exposed facet, which is beneficial for photocatalytic hydrogen generation (Figure 7c). As shown in Figure 7b, the P atom has been successfully injected into the CZIS nanobelts and evenly distributed throughout the nanoribbon. Importantly, P doping does not change the crystal structure and morphology of the CZIS nanobelts (Figure 7d). Meanwhile P doping can extend the light absorption range and upshift the VB of CZIS nanobelts (Figure 7d,e). Time-resolved photoluminescence (PL) decay spectra and optical pump THz probe spectroscopy (OPTPS) demonstrate that P doping efficiently suppresses the recombination of photogenerated carrier and enhances the rates of carrier transfer, thereby improving the photocatalytic performances (Figure 7f,g). As a result, the P-doped CZIS nanobelts exhibit a 3.5-fold higher visible-light photocatalytic hydrogen production rate than that of pristine CZIS nanobelts (Figure 7h). Additionally, the CZIS-P nanobelts exhibit remarkable stability in photocatalytic hydrogen production, as evidenced by the negligible decrease in hydrogen production rates observed after 6 consecutive cycles totaling 24 h of operation.

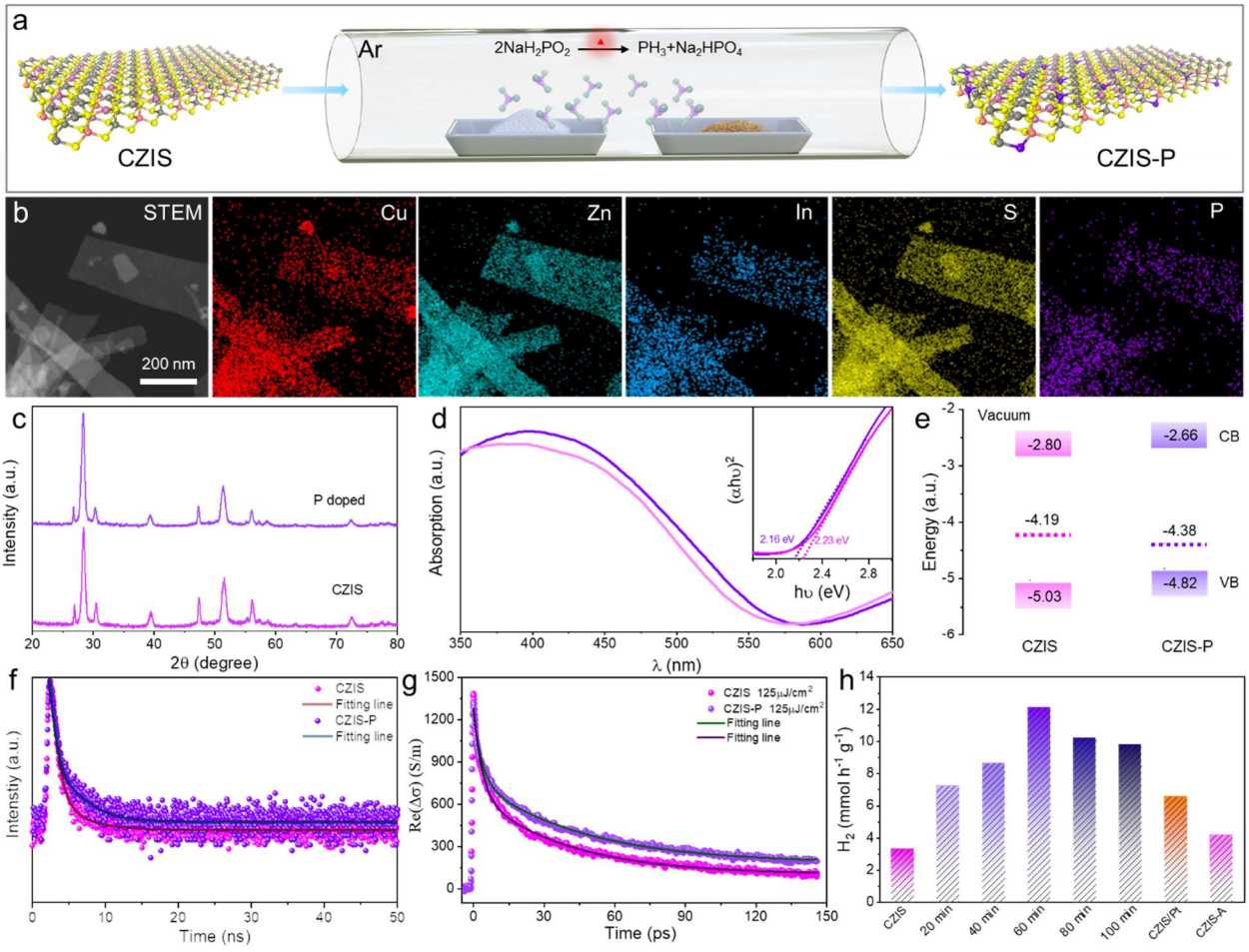

Figure 7. (**a**) The schematic diagram depicts the fabrication of CZIS-P nanobelts via an annealing process. (**b**) EDS element mapping of CZIS-P nanobelts. (**c**–**g**) XRD patterns, UV−vis absorption spectra, electric band structures, PL decay spectra, and time-resolved THz photoconductivities of P-doped and pristine CZIS nanobelts. (**h**) Photocatalytic hydrogen generation rates over

the pristine CZIS nanobelts, P-doped CZIS nanobelts synthesized at 300 °C for different times, Pt decorated CZIS nanobelts (CZIS/Pt), and CZIS nanobelts annealed at 300 °C without sodium hypophosphite monohydrate (CZIS-A) [119].

3.3. Cocatalyst Loading

Loading cocatalysts onto the semiconductor photocatalysts is one of the effective methods for improving the catalytic properties [120–122]. The incorporation of cocatalysts confers numerous advantages during the photocatalytic process [123,124]. (I) The cocatalysts can act as trap sites to capture the photogenerated carriers, thereby promoting charge separation. (II) The cocatalysts contribute to enhanced absorption of the target molecules. (III) The cocatalysts have the ability to regulate the surface reaction dynamics and modulate the activation energy for specific target molecules. (IV) By altering molecular coordination modes, the cocatalysts exert control over product selectivity. (V) Incorporation of cocatalysts in certain systems can effectively suppress photocorrosion and improve the stability of the photocatalysts. So far, a wide range of cocatalysts have been developed and used to improve the photocatalytic properties of semiconductors, including noble metal nanoparticles, transition metal oxides and sulfides, metal phosphide, and graphene [125–130].

The utilization of noble metal nanoparticles as cocatalysts is widely employed to enhance the photocatalytic performances of CQSNs [131–133]. For example, Han and the co-author decorated Pt nanoparticles on the tips of CZIS nanorods to enhance visible-light-driven photocatalytic hydrogen production [134]. Cabot and coauthors utilized Pt and Au nanoparticles as cocatalysts, strategically deposited onto WZ CZTS to enhance its photocatalytic capabilities (Figure 8a) [135]. Quasi-spherical WZ CZTS are synthesized, and served as seeds to synthesize CZTS-Pt and CZTS-Au heterostructure nanoparticles (Figure 8b,c). The addition of Pt/Au does not alter the size of CZTS nanocrystals, while preferential nucleation of Pt/Au nanocrystals occurs at the surface of CZTS nanoparticles. CZTS-Pt and CZTS-Au heterostructures showed approximately a 6-fold and 5-fold higher photodegradation rate of Rhodamine B (RHB) compared to that of pure CZTS nanocrystals, respectively (Figure 8d). Figure 8e that the loading of Pt and Au nanoparticles enhanced the photocatalytic hydrogen production rate of CZTS nanocrystals. The highest hydrogen evolution rate of CZTS-Pt with the Pt load at around 1% is 1.02 mmol $g^{-1} \cdot h^{-1}$, which is 8 times higher than that of pristine CZTS (0.13 mmol $g^{-1} \cdot h^{-1}$) (Figure 8e,f). In addition, metal sulfides can also be used as cocatalysts to enhance the photocatalytic performances of CQSNs [136]. For example, Niu and coauthors optimized the photocatalytic performance of CZTS nanoparticles by introducing ca.1 mol% of MoS_2 [137]. The MoS_2/CZTS heteronanostructures show about 7.8 times higher photocatalytic hydrogen evolution rates than CZTS nanoparticles.

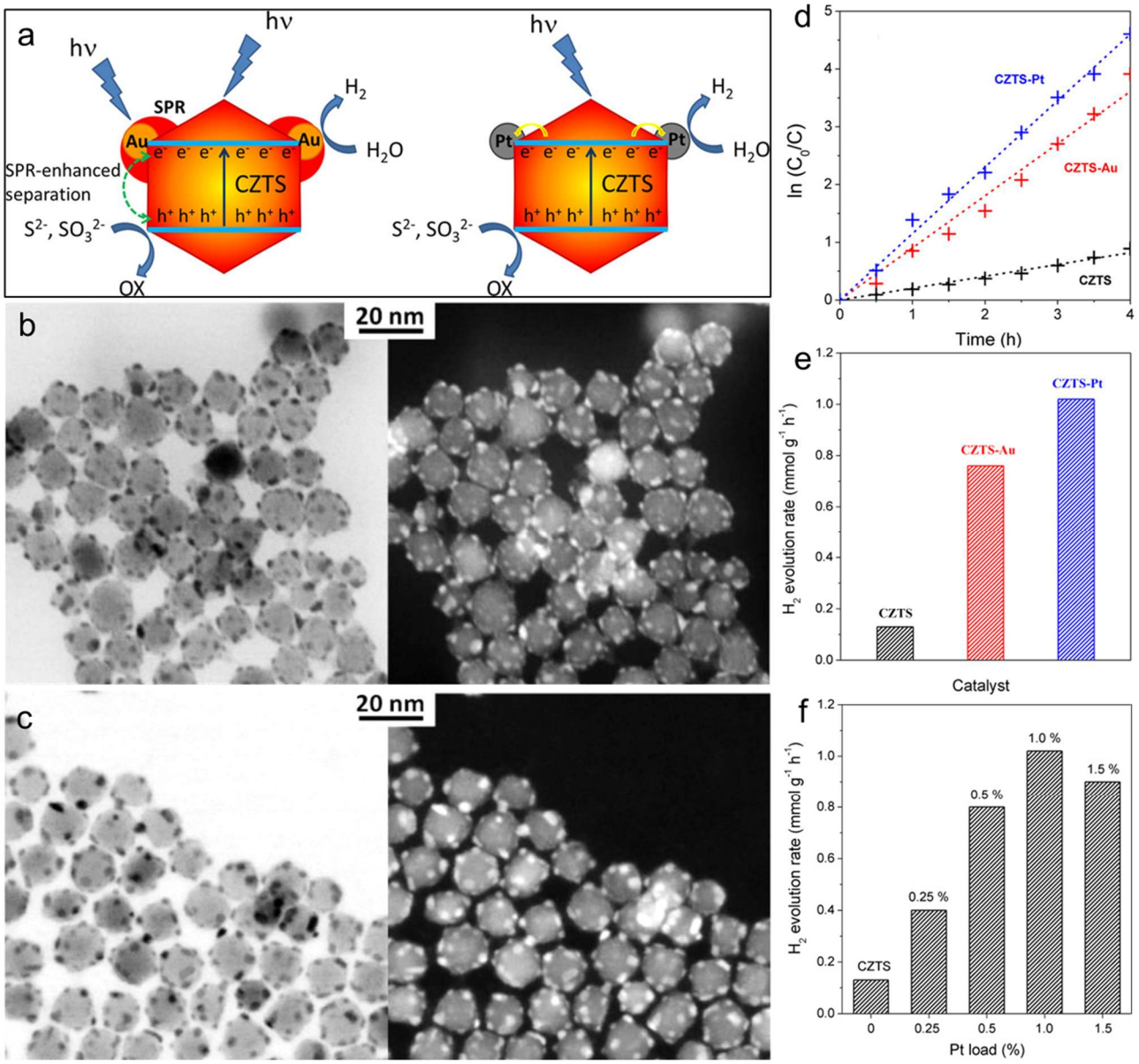

Figure 8. (**a**) Schematic illustration of the photocatalytic hydrogen generation over CZTS-Au and CZTS-Pt heterostructured nanoparticles. (**b**,**c**) Bright-field and dark-field TEM images of CZTS-Au and CZTS-Pt heteronanocrystals, respectively. (**d**) Photodegradation performances of RHB. (**e**) Comparison of photocatalytic hydrogen production performances of CZTS, CZTS-Au, and CZTS-Pt heteronanocrystals. (**f**) Photocatalytic hydrogen production performances of CZTS-Pt heteronanocrystals with varying Pt loads [135].

3.4. Vacancy Engineering

As a common point defect, atomic vacancies significantly enhance the photocatalytic performance of semiconductor catalysts by modulating their photoelectrochemical and physicochemical properties. These include extending the light absorption range, serving as active reaction sites on the surface that can trap photogenerated carriers and promote adsorption and desorption of intermediates, and adjusting the energy band structures [138–141]. Since Yanagida and coauthors first reported the sulfur vacancy engineering of ZnS to enhance its photocatalytic performance in 1998, increasing attention has been drawn to vacancy engineering in photocatalysis [142]. Recently, with the growing interest in multinary metal sulfide photocatalysts, research on vacancy engineering of CQSNs is also gaining momentum [9,55,143–145].

The wide range of cations and the crystal structure tolerance exhibited by CQSNs facilitate the formation of cation vacancies within these materials [50,146–148]. The modulation of photoelectric properties and electronic structure in semiconductors is predominantly influenced by cation vacancies rather than anion vacancies [149,150]. The literature contains numerous reports on the utilization of cation vacancy defect engineering in Cu-based quaternary chalcogenides for enhancing solar cell properties, reducing thermal conductivity, and modifying emission properties [151–154].

Recently, Wang and coauthors reported on the defect engineering of colloidal Zn-doped $CuInS_2$ (ZCIS) QDs, utilizing Cu vacancy and Cu^{2+} defect states to achieve photocatalytic CO_2 reduction. They also investigated the impact of defect−defect interactions on photogenerated carrier dynamics and photocatalytic processes [155]. The Cu-deficient and stoichiometric QDs exhibit three typical defect state types: type-A stoichiometric QDs containing antisite Cu_{In}''-$In_{Cu}^{\bullet\bullet}$ pairs, type-B Cu-deficient ZCIS QDs with Cu vacancies (V_{Cu}'), and type-C Cu-deficient ZCIS QDs with both Cu vacancies (V_{Cu}') and Cu^{2+} defect states ($Cu_{Cu}^{\bullet}$) (Figure 9a). They first used theoretical simulations to predict the CO_2 absorption capacity of the three ideal Cu defect sites (Figure 9b), revealing the affinity between Cu^{2+} defect sites close cooper vacancies and CO_2 molecules is the highest. Thus, preparing type-C Cu-deficient QDs for photocatalytic CO_2 reduction is desirable. Then, type-A stoichiometric colloidal QDs were prepared and denoted as 8/12ZCIS, and the Cu-deficient QDs, including 4/12ZCIS, 2/12ZCIS, and 1/12ZCIS, were produced by changing the atomic Cu/In ratios. The 2/12ZCIS sample has the highest EPR signal intensity tested, indicating the most abundant vacancy defects in this QD (Figure 9c). The Cu-deficient 2/12ZCIS sample exhibited the highest photocatalytic activity for the reduction of CO_2 to CO with a rate of 0.4–0.5 mmol h^{-1} g^{-1} (Figure 9d–f). However, the presence of Cu vacancy defect may lead to unexpected charge recombination and consequently diminish the photocatalytic performances. For example, Ning and coauthors used Zn to effectively mitigate surface defects and unexpected recombination of carriers of CIS QDs. Consequently, the obtained CZIS QDs exhibit excellent photocatalytic hydrogen production performances in both the visible and near-infrared regions [40].

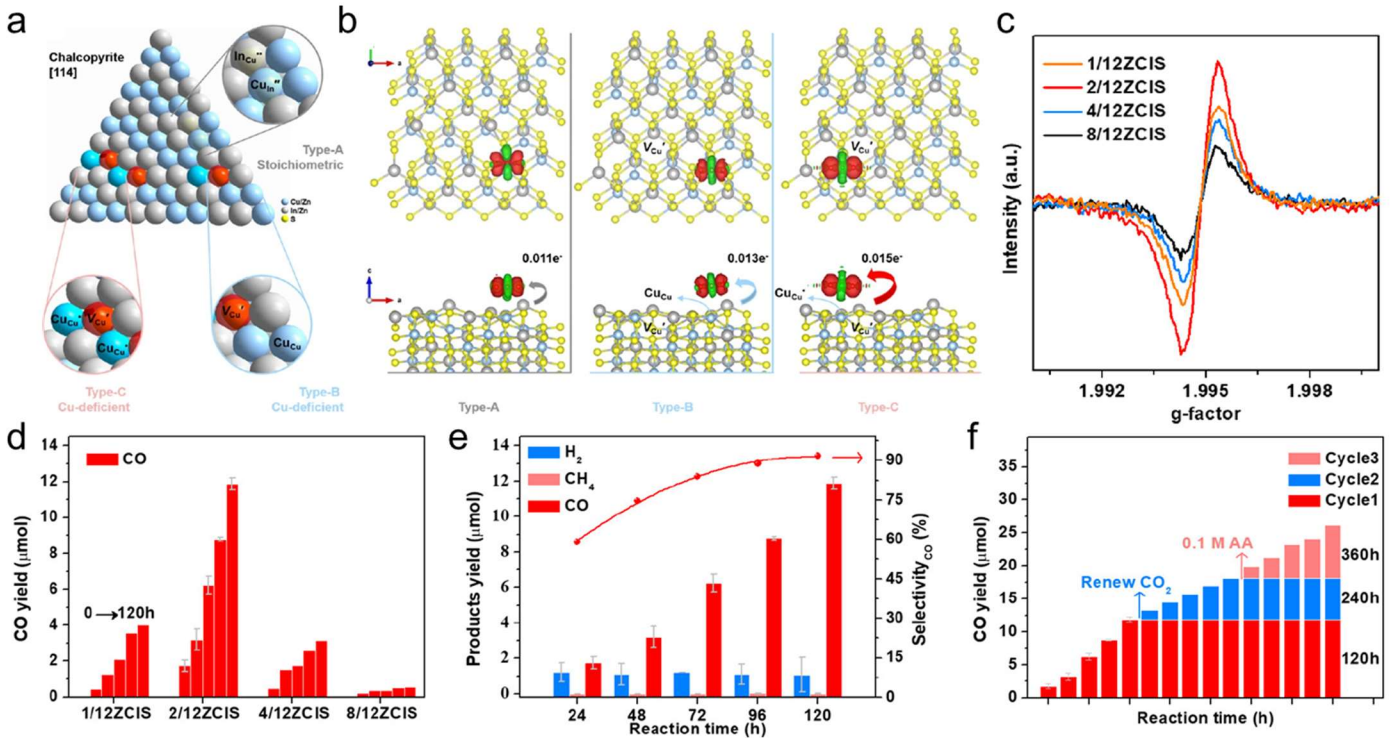

Figure 9. (**a**) Schematic illustration of the different defect state types in Cu-deficient and stoichiometric ZCIS QDs. (**b**) The hypothetical CO_2 adsorption allocation on type-A stoichiometric, type-B Cu-deficient, and type-C Cu-deficient ZCIS QDs, respectively. (**c**) EPR spectra of the synthesized ZCIS QDs. (**d**–**f**) Photocatalytic CO_2 reduction performances of ZCIS QDs [155].

3.5. Interface Engineering

Due to the rapid recombination of photogenerated carriers and low electron utilization, the photocatalytic performance of CQSN photocatalyst is insufficient for practical applications. To overcome these drawbacks of unmodified single semiconductor photocatalysts, fabricating heterojunction interfaces by coupling two kinds of different semiconductors is an effective and widely used strategy to extend the light absorption range and promote the separation and transfer of photogenerated carriers, thereby improving their photocatalytic performances [156–159]. Generally, based on the band alignments and carrier transfer pathways, type II heterojunctions are 、 considered optimal for efficient separation and transfer of photogenerated carriers [160–162].

The construction of efficient heterojunction photocatalysts relies on two crucial factors: electronic band structure matching and geometric configuration matching [163,164]. Based on these principles, diverse heterostructured

photocatalysts have been designed and developed to realize efficient solar-to-chemical energy conversions [157,165–167]. In recent years, CQSN-based heterostructured photocatalysts have been synthesized for energy and environmental applications [70,168,169]. For example, Wu and coauthors have synthesized CZTS-CdS heterostructured nanoparticles for photocatalytic hydrogen evolution [170]. When CdS comes into contact with CZTS nanocrystals, a p-n heterojunction with a built-in electric field is formed, facilitating the transfer of electrons from CZTS to CdS (Figure 10a). They fabricated CZTS-CdS heterostructured nanocrystals through a two-step method. After 3 cycles of CdS grew, the average diameter of CZTS-3CdS nanoparticles increased to 12 nm, and their morphology changed from quasi-sphere to quasi-square (Figure 10b). The HRTEM reveals distinct lattice fringes at the periphery of CZTS-3CdS heterostructured nanocrystal, exhibiting an interplanar spacing of 0.33 nm corresponding to (111) plane of cubic CdS (Figure 10c). The two peaks located at 604 and 299 cm^{-1} in the Raman spectrum of CZTS-3CdS heterostructured nanocrystals proved the existence of CdS (Figure 10d). The photocatalytic performances of CZTS-xCdS heterostructured nanocrystals were found to be enhanced with increasing CdS thickness. Among the heterostructures, CZTS-3CdS heterostructured nanocrystals possess the highest photocatalytic hydrogen production rate of 937.6 μmol g^{-1} h^{-1} (Figure 10e), which is 15-fold higher than the original WZ CZTS (64.5 μmol g^{-1} h^{-1}) and 31 times as high as CdS (30.2 μmol g^{-1} h^{-1}), respectively. However, if the thickness of CdS exceeded a certain limit (more than 3 cycles), it could potentially restrict the utilization of visible light by the CZTS core and impede electron transfer, resulting in a reduction in the rate of photocatalytic H_2 evolution. Furthermore, the CZTS-3CdS heterostructured nanocrystals exhibit exceptional stability (Figure 10f). Zhou and co-author decorated CdS nanorods with CZTS nanocrystals to prepare CZTS-CdS 0D/1D heterostructures [171]. The hydrogen evolution rate of the obtained 0D/1D heterostructures was 165 times higher than that of individual CZTS nanoparticles and 48 times higher than that of individual CdS nanorods, respectively.

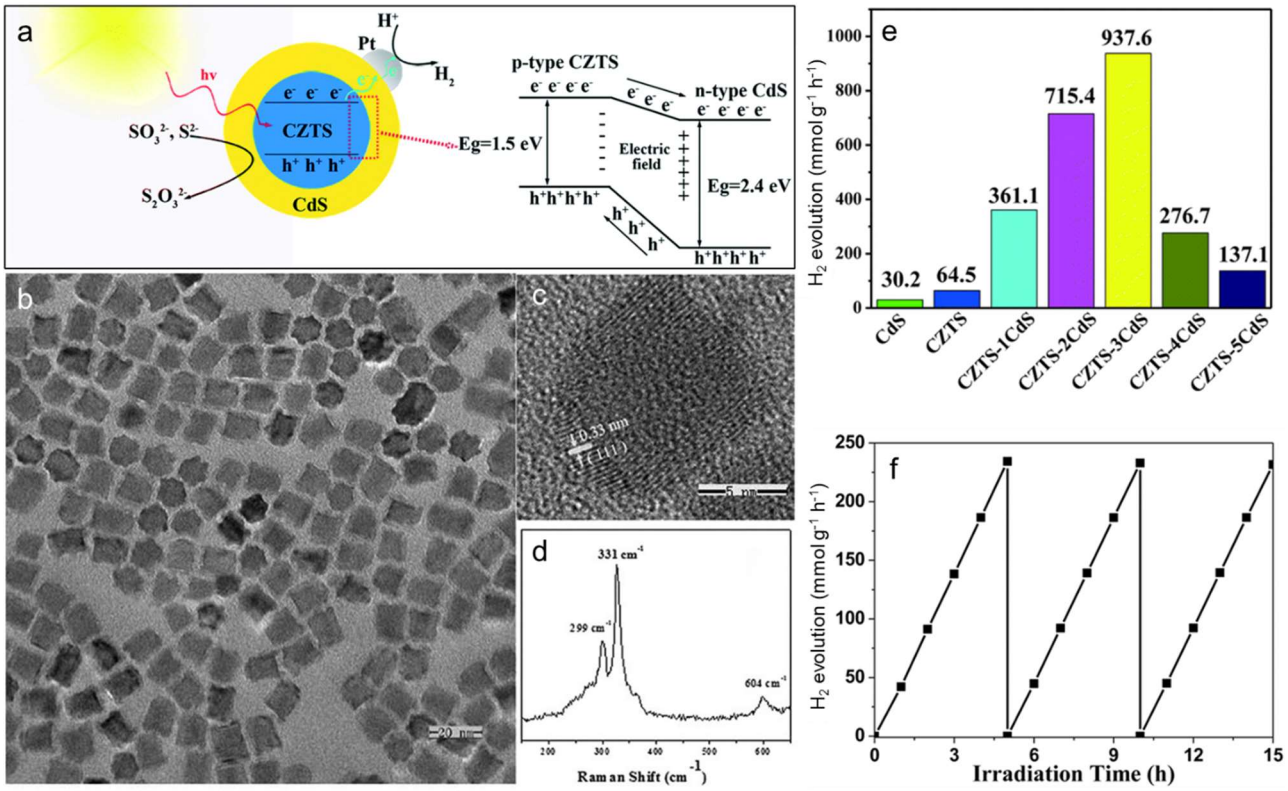

Figure 10. (**a**) Schematic illustration of band structure alignment and photogenerated carrier separation in CZTS-CdS heterojunction. (**b**,**c**) TEM and HRTEM images of CZTS-CdS heteronanocrystals. (**d**) The Raman spectrum of CZTS-CdS heteronanocrystals. (**e**,**f**) Photocatalytic performances of the synthesized CZTS-CdS heteronanocrystals [170].

However, the defects and interface stresses resulting from changes in composition and lattice mismatch at the heterojunction restrict the separation and migration of photogenerated carriers, posing limitations on photocatalytic reaction. On the other hand, constructing a homojunction interface using chemically identical but structurally different materials can avoid these troubles associated with compositional change and lattice mismatch at the heterointerfaces, facilitating efficient photogenerated carrier separation and efficient solar-to-hydrogen conversion [172–175]. There are two typical crystal phases of chalcogenide semiconductors: WZ and ZB structures. The atoms in the ZB structure are arranged in an ABCABC manner in the [111] direction, and the atoms in the WZ structure are stacked in an ABABAB manner in the [0001] direction.

Due to the small energy difference between WZ and ZB and the tiny mismatch of the $(111)_{ZB}$ and $(0001)_{WZ}$ facets, WZ and ZB can be linked together along the $[111]_{ZB}$ and $[0001]_{WZ}$ directions to form a polytype.

Alex Zunger and coauthors calculated the energy difference between WZ and ZB structures in II-VI semiconductors and predicted the existence of polymorphic structures in II-VI compounds in 1992 [176]. Subsequently, more and more scientists are paying attention to polytypic nanocrystals. In recent years, diverse colloidal polytypic Cu-based multinary chalcogenide nanocrystals have been designed and successfully synthesized [177–181]. We have developed a simple colloidal method to prepare a polytypic CQSNs library (Figure 11a) [182]. The homojunction number in polytypic CZTS nanocrystals can be precisely regulated by adjusting the amount of 1-DDT. Bullet-shaped single-homojunction polytypic (SHP) CZTS nanocrystals featuring a WZ section and a KS cusp were synthesized using 1 mL of 1-DDT.Rugby-shaped double-homojunction polytypic (DHP) CZTS nanocrystals with one WZ part and two opposite KS cusps are produced via using 0.5 mL of 1-DDT. The bandgaps of SHP and DHP CZTS nanocrystals are 1.51 and 1.47 eV, which are suitable for visible-light absorption (Figure 11b). The photocatalytic hydrogen evolution rate of the SHP and DHP CZTS nanocrystals are 2.8-fold and 3.9-fold than that of the KS CZTS nanocrystals, respectively (Figure 11c). In addition, the polytypic CZTS nanocrystals exhibited high stability against photocorrosion (Figure 11d). The DFT calculations illustrated that the homojunction formed with KS and WZ exhibited a type II band alignment, leading to the accumulation of photogenerated electrons in KS and holes in WZ. This facilitates charge separation across the homojunction, enhancing photocatalytic properties (Figure 11e–g).

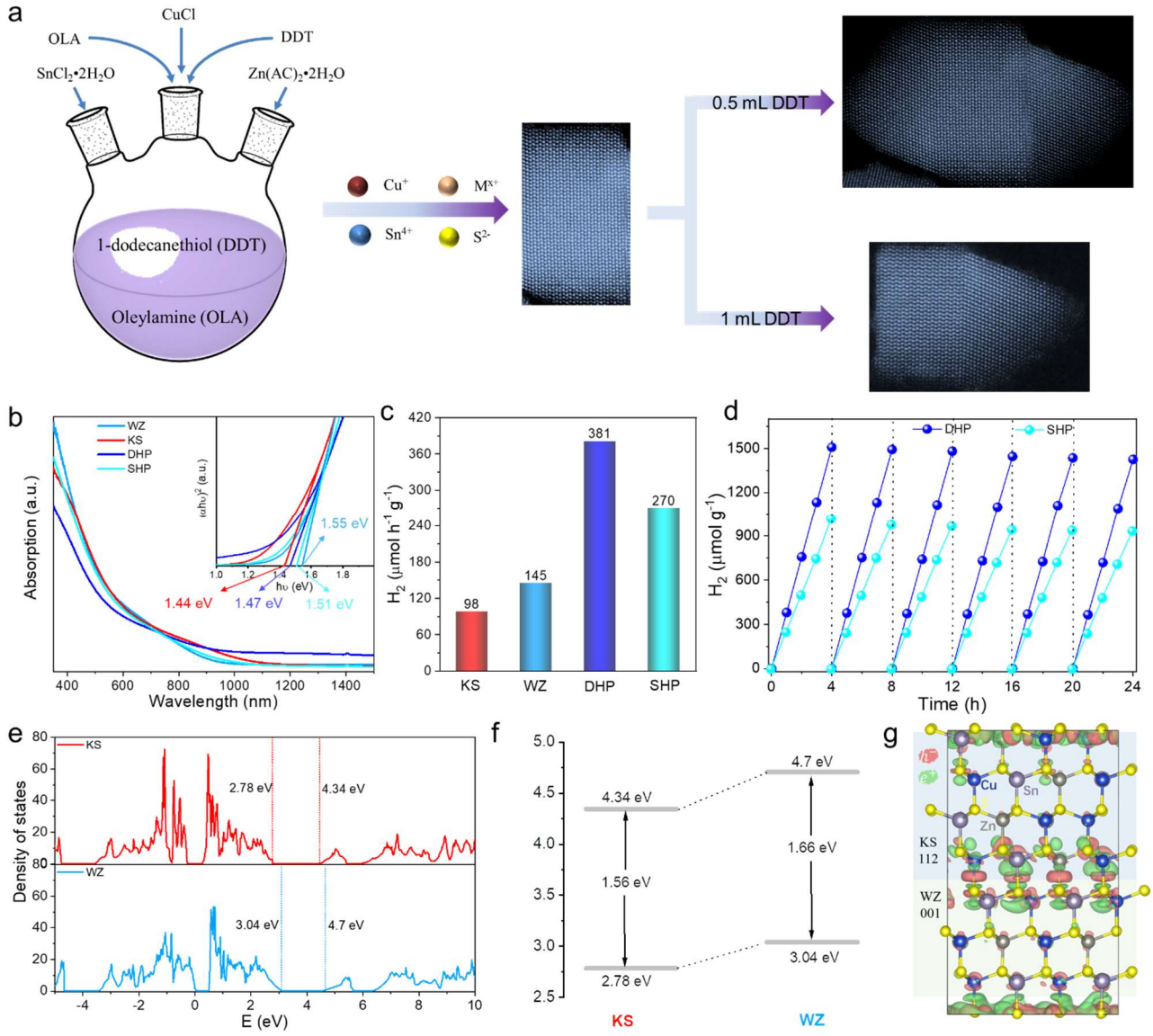

Figure 11. (**a**) Schematic illustration for synthesizing SHP and DHP CZTS nanocrystals. (**b**–**d**) Absorption and photocatalytic hydrogen production properties of phase-pure and polytypic CZTS nanocrystals. (**e,f**) The calculation of DOS and bandgap alignments of WZ and KS phases in the polytypic structures. (**g**) The simulated charge distributions in the homojunction [182].

4. Photocatalytic Applications of Cu-Based Quaternary Nanomaterials

Due to their appropriate band gap, CQSN photocatalysts have shown great potential in various photocatalytic applications. The fundamental principle of a photocatalytic reaction is very simple. The photocatalysts absorb light, exciting electrons to the CB while leaving holes in the VB. Subsequently, the photogenerated electrons in the CB transfer to the surface of the photocatalyst and take part in reduction reactions such as hydrogen production and CO_2 reduction. Simultaneously, the remaining holes in VB participate in oxidizing reactions such as oxygen evolution and oxidation of organics [183–185]. In this section, we provide a summary of the photocatalytic applications of CQSNs, including photocatalytic water splitting to produce hydrogen, PEC hydrogen production, CO_2 reduction, organic synthesis, and pollutant removal.

4.1. Photocatalytic Hydrogen Production

Due to its multiple usage modes, high specific energy, and clean reaction products, hydrogen has emerged as a promising candidate for future energy sustainability. Solar-driven hydrogen evolution via semiconductor photocatalysts is regarded as a green and sustainable hydrogen production method, garnering extensive research attention [186–188]. To date, a variety of semiconductor photocatalysts have been designed and utilized for solar-to-hydrogen conversion [19,124,189]. Among these photocatalysts, CQSNs are favored for photocatalytic hydrogen production due to their excellent stability, non-toxicity, and broad absorption range in the visible light spectrum [35,37,190,191].

Since the groundbreaking work on photocatalytic hydrogen evolution over CZIS solid solution under visible-light irradiation was reported by Kudo and coauthors in 2005 [41], significant efforts have been dedicated to this research field. CQSNs play a critical role in solar-to-hydrogen conversion; however, their efficiency is constrained by inadequate separation and utilization of photogenerated carriers. Shi and coauthors designed a ternary photocatalyst comprising CIZS QDs, MoS_2, and carbon dots (CDs) for efficient solar-driven photocatalytic hydrogen production [192]. CZIS QDs with a size distribution of about 4.5 ± 0.5 nm and CDs with a size distribution of about 2.5 ± 0.5 nm are synthesized first and then attached to the surface of MoS_2 nanosheets to form a ternary CZIS/NoS_2/CDs 0D/2D heterostructured composite (Figure 12a–d). Moreover, the EDX-elemental mapping images of CIZS/MoS_2/CDs exhibited the uniform distribution of Cu, In, Zn, S, Mo, C, N, and O elements, clarifying that the CIZS QDs and CDs were successfully attached and well dispersed on MoS_2 nanosheets (Figure 12e). The impact of MoS_2 and CDs on the photocatalytic activity of CZIS QDs was investigated by varying their loading amounts to determine the optimal load. The rate of photocatalytic hydrogen production increased with increasing loading amount of MoS_2, reaching a maximum value at 1.663 mmol h^{-1} g^{-1} (CZIS-MoS_2-5%), which was 2.98 times higher than that of the pristine CZIS (Figure 12f). Then, the effect of CDs was further investigated in detail, varying their loading amounts on CIZS/MoS_2-5%. The optimized CIZS/MoS_2/CDs photocatalysts exhibited a hydrogen evolution rate of 3.706 mmol h^{-1} g^{-1}, which was 6.65 times and 148.24 times higher than that of the original CIZS and MoS_2, respectively (Figure 12g,h).

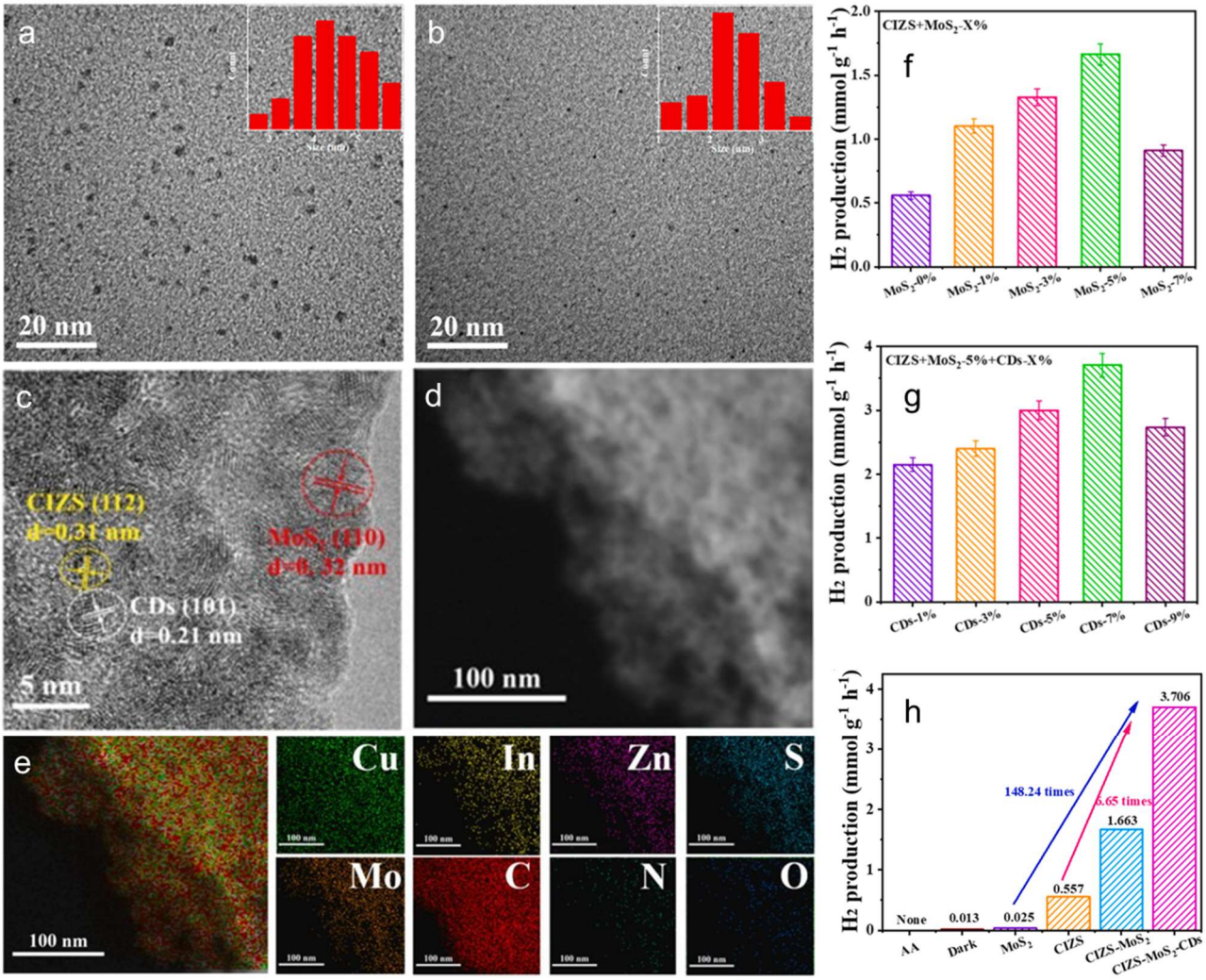

Figure 12. (**a**,**b**) TEM images of CZIS QDs and CDs, respectively. (**c**–**e**) HRTEM, HAADF-STEM, and EDX-elemental mapping images of CIZS/MoS_2/CDs. (**f**–**h**) Photocatalytic hydrogen production performances of CZIS/MoS_2 and CIZS/MoS_2/CDs [172].

Except for the 0D CQSNs, successful synthesis and utilization of 1D, 2D, and 3D CQSNs have been achieved for photocatalytic hydrogen production. For example, 1D WZ CZIS nanorods were synthesized via a one-pot non-injection method and subsequently functionalized with Pt and Pd_4S cocatalysts to improve photocatalytic performances [134]. The introduction of Pt and Pd4S resulted in a remarkable improvement in the photocatalytic properties of CZIS by approximately 3.5-fold and 3-fold, respectively. Wang and coauthors prepared 2D graphene-like ultrathin CZTS nanosheets for highly stable photocatalytic hydrogen production [193]. The ultrathin CZTS nanosheets with a 2–3 nm thickness exhibit a high hydrogen evolution rate of 1.5 mmol h^{-1} g^{-1}. Chen and coauthors synthesized 3D CZIS hollow sub-microspheres for efficient visible-light-driven photocatalytic hydrogen evolution [58]. The highest hydrogen evolution rate reaches 3.79 mmol h^{-1} g^{-1} for RuS_x decorated CZIS hollow sub-microspheres.

4.2. Photoelectrochemical Hydrogen Production

Photoelectrochemical hydrogen evolution is an efficient method for producing hydrogen [194–196]. PEC water splitting, using commonly employed photovoltaic materials like Si, TiO_2, and CdTe, has achieved significant advancements [197–199]. Meanwhile the high energy fabrication process of Si, the narrow light absorption range, and the toxicity of Cd in CdTe hindered their large-scale applications in PEC water splitting. Recently, Cu-based quaternary chalcogenides have emerged as promising photocathode materials for PEC water splitting, owing to their excellent photovoltaic performance in thin-film solar cells [45,200–203]. In recent years, a variety of CQSNs have been utilized in the fabrication of photoelectrodes for PEC hydrogen production [204–206]. For example, Silvula and coauthors used CZTS colloidal inks to prepare thin-film photocathodes, which exhibited excellent PEC performances [207]. Kudo and co-author fabricated a PEC cell with a CoO_x-modified $BiVO_4$ photoanode and a Ru-loaded $(CuGa)_{0.5}ZnS_2$ photocathode for water splitting without applying an external bias, which exhibited excellent performances [208].

Wide-bandgap metal oxides (e.g., TiO_2 and ZnO) are widely utilized as anode materials for efficient PEC hydrogen production [209,210]. However, metal oxides limited visible light absorption hinders their solar-to-hydrogen conversion. Sensitizing metal oxides with quantum dots, particularly CQSN CDs, is one of the most effective strategies to expand the light absorption range and thereby enhance PEC performance [211–214]. Kim and coauthors developed a green chemistry method wherein vegetable oil is used as a non-toxic solvent to produce monodisperse and size-tunable CZTS nanocrystals. Then, a 5 nm thin atomic Zn(O,S) layer is covered onto previously prepared TiO_2 nanorod arrays (TNR) to prepare Zn(O,S)/TNR electrode. Lastly, the obtained CZTS nanocrystals are deposited onto Zn(O,S)/TNR electrode to fabricate a ternary CZTS NCs/Zn(O,S)/TNR photoelectrode for PEC water splitting [215]. As shown in Figure 13a,b, the TNRs are fully encapsulated by Zn(O,S) and CZTS nanocrystals. The formation of sequence type-II heterojunctions between CZTS, Zn(O,S), and TNR promotes efficient photogenerated carrier separation, thereby enhancing PEC performances (Figure 13c).

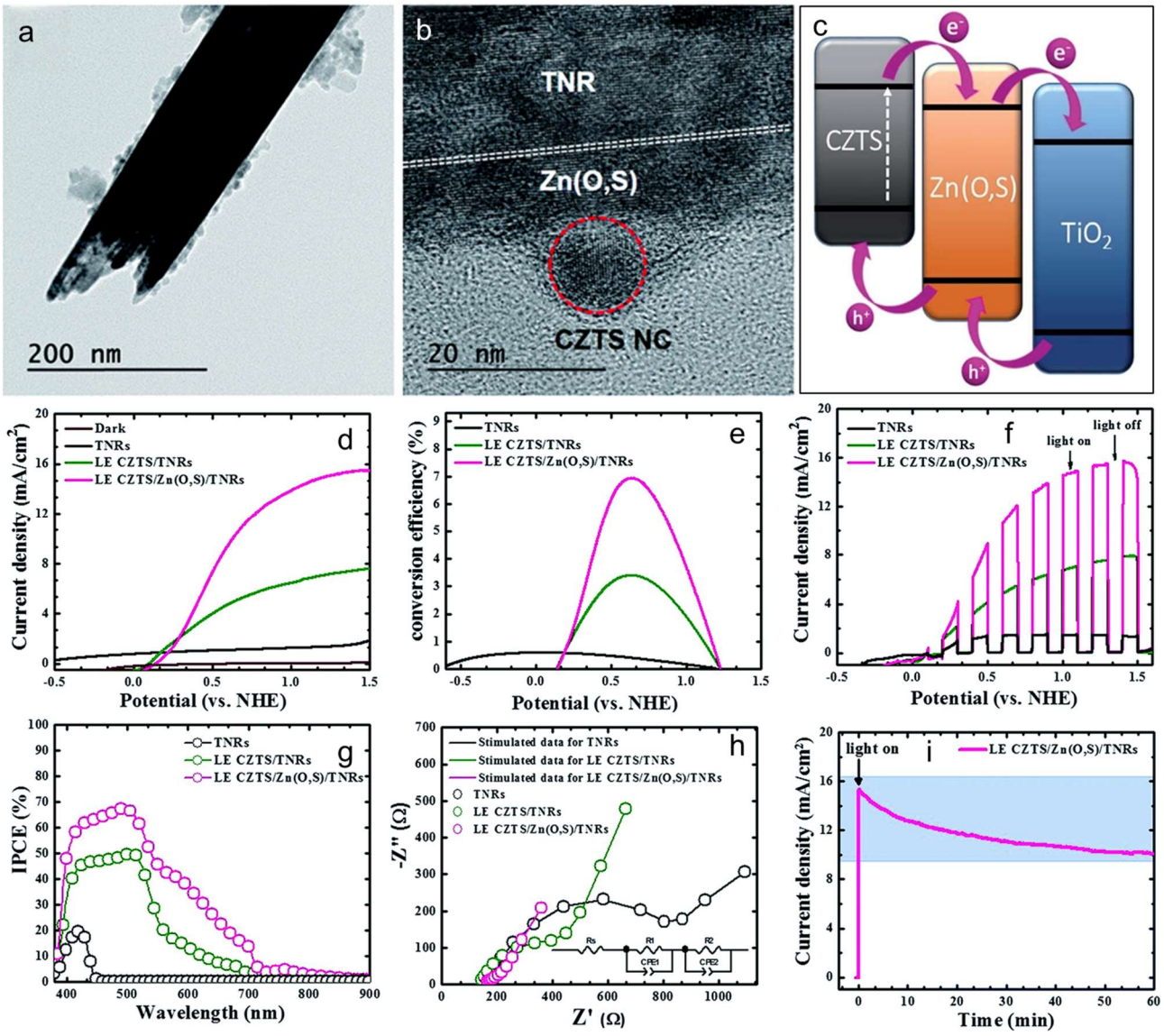

Figure 13. (**a**,**b**) TEM and HRTEM of the CZTS NCs/Zn(O,S)/TNR structure. (**c**) Illustration of the charge transfer mechanism. (**d**–**h**) Photocurrent densities-voltage (J-V) curves under dark and illumination, STH efficiency-voltage curves, chopped on/off cycles, incident IPCE as a function of wavelength, and EIS spectra of TNR, LE CZTS/TNR, and LE CZTS/Zn(O,S)/TNR. (**i**) Photocurrent-time (I-t) curves of LE CZTS/Zn(O,S)/TNRs [215].

The ligand exchange (LE) CZTS/TNRs, LE CZTS/Zn(O,S)/TNRs and TNRs are used as photoelectrodes for PEC measurements. All the photoelectrodes exhibit a negligible dark current (Figure 13d), a reproducible and rapid photocurrent response and the light on/off (Figure 13f). The LE CZTS/Zn(O,S)/TNR photoelectrode shows an extraordinary photocurrent density of 15.05 mA cm^{-2} at 1.23 V (vs. the NHE), which is much higher than that of TNR photoelectrode (1.39 mA cm^{-2}) and LE CZTS/TNR photoelectrode (7.13 mA cm^{-2}) at 1.23 V (vs. the NHE) (Figure

13d). The LE CZTS/Zn(O,S)/TNR photoelectrode shows the highest photo conversion efficiency of 6.94% at 0.64 V (vs. the NHE), which is about 11.4 and 2 times that of TNRs (0.61% at 0.043 V) and LE CZTS/TNRs (3.40% at 0.62 V), respectively (Figure 13e). The LE CZTS/Zn(O,S)/TNR photoelectrode shows a greater IPCE in the visible region with the highest IPCE of 69.42% at 510 nm (Figure 13g). The electrochemical impedance spectroscopy (EIS) studies demonstrated that the LE CZTS/Zn(O,S)/TNR photoelectrode exhibited the lowest R_{CT} value (Figure 13h), suggesting the more effective separation of photogenerated carriers and the lowest charge transfer resistance, and thus exhibiting the best PEC performances. Additionally, the photocurrent of LE CZTS/Zn(O,S)/TNR photoelectrode showed a marginal decrease and maintained approximately 67% of its original value after 60 min (Figure 13i).

4.3. Photocatalytic CO_2 Reduction

CO_2—a greenhouse gas—has caused serious environmental issues. Reducing CO_2 to hydrocarbon fuels (e.g., methane and formate) is a potential strategy to alleviate this trouble. Inspired by photosynthesis, solar-energy-driven photocatalytic reduction of CO_2 to hydrocarbon fuels emerges as a promising approach that simultaneously reduces greenhouse gas emissions and addresses global energy demands. Extensive research has been conducted on various photocatalysts for this purpose, including metal nitrides, polymers, metal oxides and metal sulfides [7,216–219]. Among them, metal sulfides exhibit excellent performances during the photocatalytic CO_2 reduction because the sulfur has light-effective mass carriers, as well as the S 3p orbital occupies the less positive VB, resulting in an extended photorespense range and higher carrier concentration for metal sulfides [220–222]. CQNSs have been widely used for photocatalytic CO_2 reduction [70,223–227].

Recently, Chang and coauthors employed a gel-assisted method to synthesize CIZS for visible-light photocatalytic CO_2 reduction [228]. When Ru was utilized as the cocatalyst, the CIZS nanocrystals exhibited commendable reducibility in CO_2 photocatalysis, resulting in a methane, hydrogen, and formate product mixture. Zhang and coauthors found that $CuInSnS_4$ (CITS) octahedral nanocrystal photocatalyst with exposed (111) plane possesses selective capability in reducing CO_2 to methane [229]. They successfully prepared CITS nanocrystals using a simple one-step hydrothermal method. The resulting CITS features a cubic spinel crystal structure and exhibits an octahedral morphology with a size of approximately 30 nm (Figure 14a). Furthermore, the HRTEM image (Figure 14b) and SAED pattern (Figure 14c) illustrate the obtained CITS nanocrystal has high-quality exposed (111) crystal facets. As shown in Figure 14d, the absorption band edges of In_2S_3, SnS_2, Cu_2S, and CITS nanocrystals are 641.6 nm, 552.7 nm, 747.0 nm, and 787.5 nm, which corresponds to the band gap of 1.93 eV, 2.24 eV, 1.66 eV, and 1.57 eV, respectively. The electronic band energies (Figure 14e) are calculated and illustrate that both CITS and single metal sulfide nanocrystals have the ability to reduce CO_2 to CO and CH_4 under solar irradiation. Under visible-light irradiation, CITS nanocrystals exhibited excellent photocatalytic performances and photocatalyzed the reduction of CO_2 into the main products of CH_4 (Figure 14f). The main product is CO on the corresponding individual In_2S_3, SnS_2, and Cu_2S (Figure 14f). Also, the CITS nanocrystals exhibited a good photocatalytic reduction of CO_2 performance with negligible activity decrement after three-cycle tests of a total of 27 h (Figure 14g). The photocatalytic activity obviously decreases with the wavelength of the incident light increasing (Figure 14h). Meanwhile, the GC-MS spectra prove that only CH_4 is produced in the CITS photocatalyzed CO_2 reduction. The non-metal sulfur atom in the CITS photocatalysts serves as the adsorption center, specifically targeting the carbon atom of CO_2 rather than general metal or defect sites. Consequently, this selective adsorption on the non-metal sulfur atom of CITS facilitates the stabilization of intermediates and thus boosts the reduction of CO_2 to CH_4.

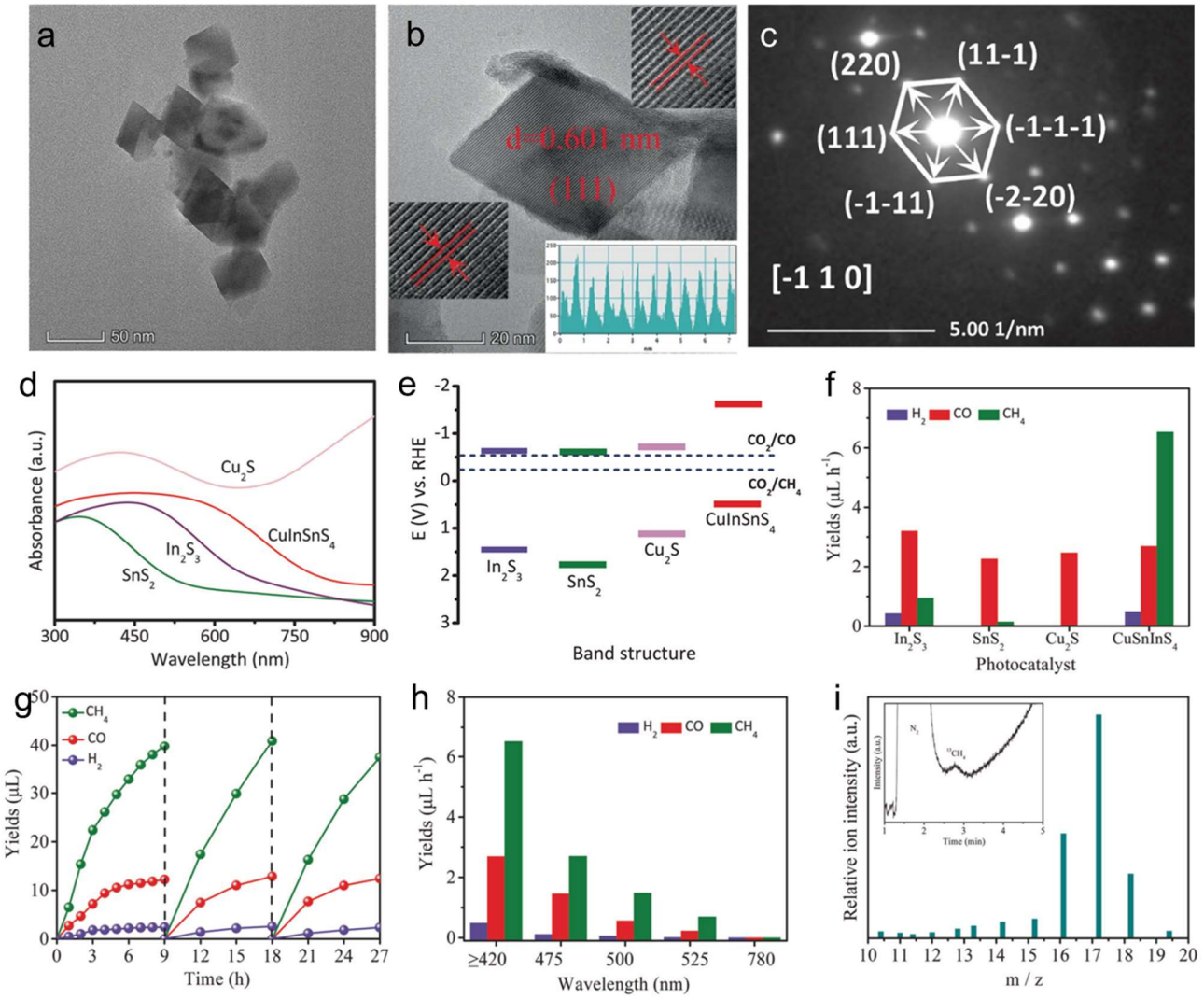

Figure 14. (**a**–**c**) TEM image, HRTEM image, and SAED pattern of CITS nanocrystals. (**d**,**e**) Absorption properties and the optical band gap energy of In_2S_3, SnS_2, Cu_2S and CITS nanocrystals. (**f**) Comparison of the photocatalytic CO_2 reduction properties over In_2S_3, SnS_2, Cu_2S and CITS nanocrystals. (**g**,**h**) Photocatalytic CO_2 reduction stability and photocatalytic performance of CITS nanocrystals under monochromatic light irradiation. (**i**) GC-MS spectra [229].

4.4. Photocatalytic Organic Synthesis

Photocatalytic organic synthesis offers an attractive approach for solar-to-chemical energy conversion and is an alternative to traditional high-energy chemical synthesis. Many classic reactions, including hydrogenation, alcohol oxidation, aerobic coupling, and epoxidation, have been carried out through photocatalytic reactions [230–234]. Due to their special light absorption properties, Cu-based quaternary sulfides are widely utilized for photocatalytic organic synthesis, such as PEC ammonia synthesis from NO_x reduction and methylcyclohexane synthesis from toluene [235,236].

CQSNs have been prepared for photocatalytic organic synthesis with the development of nanotechnology. For example, Pandey and coauthors reported the utilization of $CuAlS_2$/ZnS (CAZS) QDs for photocatalytic synthesis of organics from aqueous bicarbonate ions [237]. Biocompatible CAZS QDs were prepared for photocatalytic organics synthesis. The resulting CAZS QDs have an elongated morphology with a mean aspect ratio of 1:2.2 (Figure 15a). The distinct phase contrast within each QD indicates the presence of separate regions of $CuAlS_2$ and ZnS(Figure 15b). The HRTEM and the corresponding Fourier transform pattern also imply that CAZS QDs are core/shell materials (Figure 15c,d). The resulting QDs were used as a photocatalyst to reduce bicarbonate ions under visible light, producing both oxidizing and reducing products (O_2 and formate) over time(Figure 15f–i). The CAZS QDs exhibited an unheard-of visible light-driven photocatalytic activity for reducing carbon dioxide in the aqueous sodium bicarbonate without cocatalyst or sacrificial reagent. Additionally, devices utilizing these QDs exhibit exceptional energy conversion efficiencies, reaching up to 20.2 ± 0.2%.

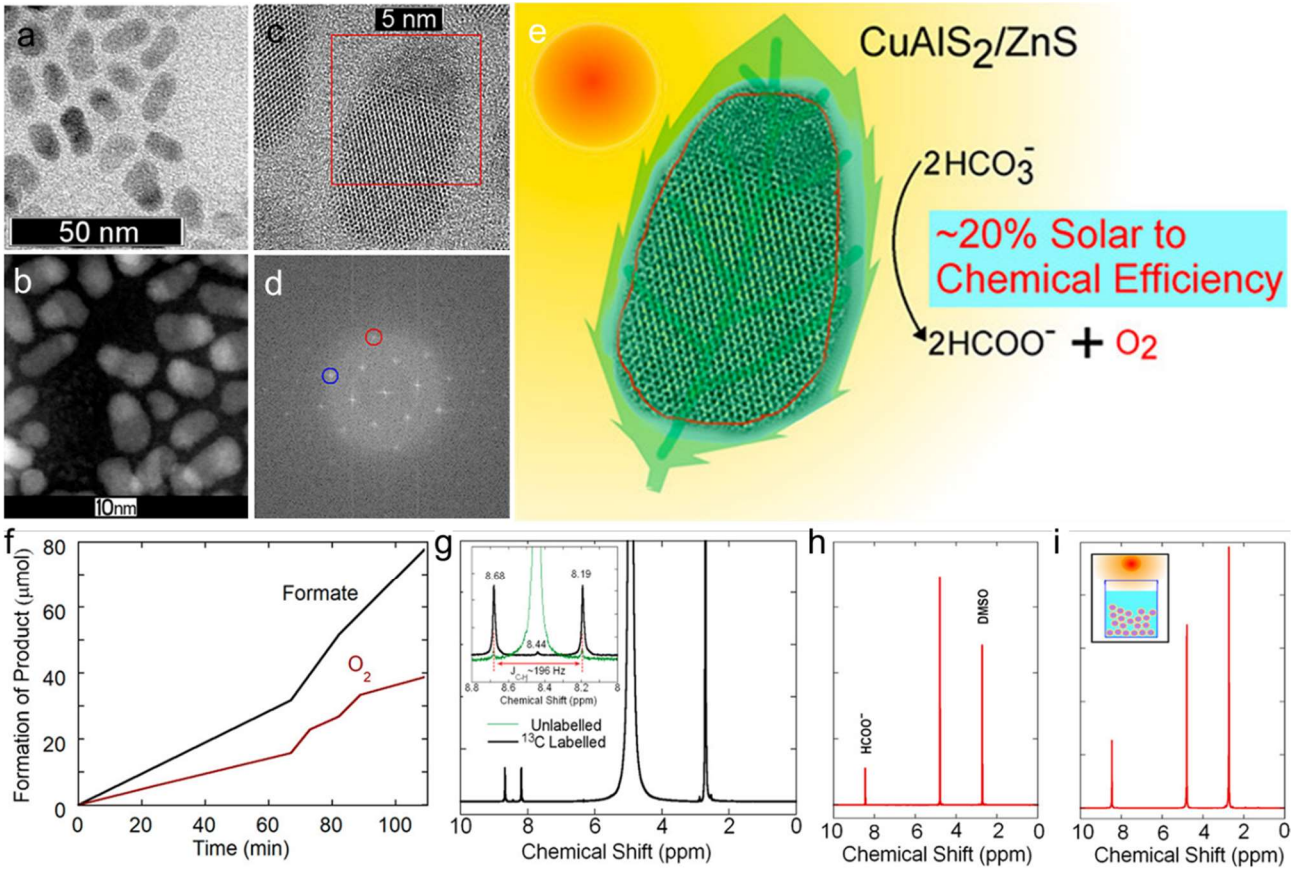

Figure 15. (**a**–**d**) TEM image, STEM image, HRTEM image, and SAED pattern of CuAlZnS nanocrystals. (**e**) Schematic illustration of the visible light photosynthesis of organic from aqueous bicarbonate ions. (**f**) Production of O_2 and formate with time by photoreduction of $NaHCO_3$. (**g**–**i**) 1H NMR of photoreduction product, a reaction mixture, and the products formed by illuminating a light-harvesting device [237].

4.5. Photocatalytic Pollutant Removal

Contemporarily, the issue of environmental pollutants has become increasingly severe due to industrialization. Solar-driven photocatalytic pollutant removal is considered an economical and effective approach to deal with this environment trouble [112,238,239]. Under visible light irradiation, semiconductor photocatalysts absorb light to produce excitons (electrons and holes), and then distinct reactive oxygen species are generated, such as •OH, $O_2^{\bullet-}$, singlet oxygen molecules ($^1O_2$), etc. Photogenerated holes and $O_2^{\bullet-}$ are the key active species over the semiconductor photocatalysts. Metal oxide and sulfide semiconductors are widely employed as photocatalysts for photocatalytic reduction of pollutants [76,240]. In recent years, CQSNs have gained significant attention from researchers as a potential solution for addressing pollution issues [241–244].

CZTS nanocrystals are widely used in the photocatalytic degradation of organic pollutants and in industrial wastewater treatment [245,246]. Acharya and coauthors used the quaternary CuZnFeS (CZFS) nanocrystals as catalysts for degrading multiple refractory organic pollutants [247]. A remarkably fast and facile synthesis route produced colloidal CZFS nanocrystals in just 30 s. The obtained mostly faceted spherical CZFS NCs have an average size of 14 ± 3 nm (Figure 16a,b). Then, the organic ligands on the NCs are exchanged with hydrazine before photocatalytic applications. The internal energy levels of hydrazine-capped CZFS (H-CZFS) extracted using scanning tunneling spectroscopy and ultraviolet photoelectron spectroscopy show that the H-CZIS nanocrystals have suitable redox potential of oxidative species (Figure 16c–e). The H-CZIS nanocrystals exhibit excellent photocatalytic properties for the degradation of multiple refractory organic pollutants (Figure 16f). Moreover, a small amount of H-CZIS nanocrystal can speed up the conversion rate of 4-nitrophenol (4-NP) to 4-aminophenol (4-AP) at a much faster rate (Figure 16g,h).

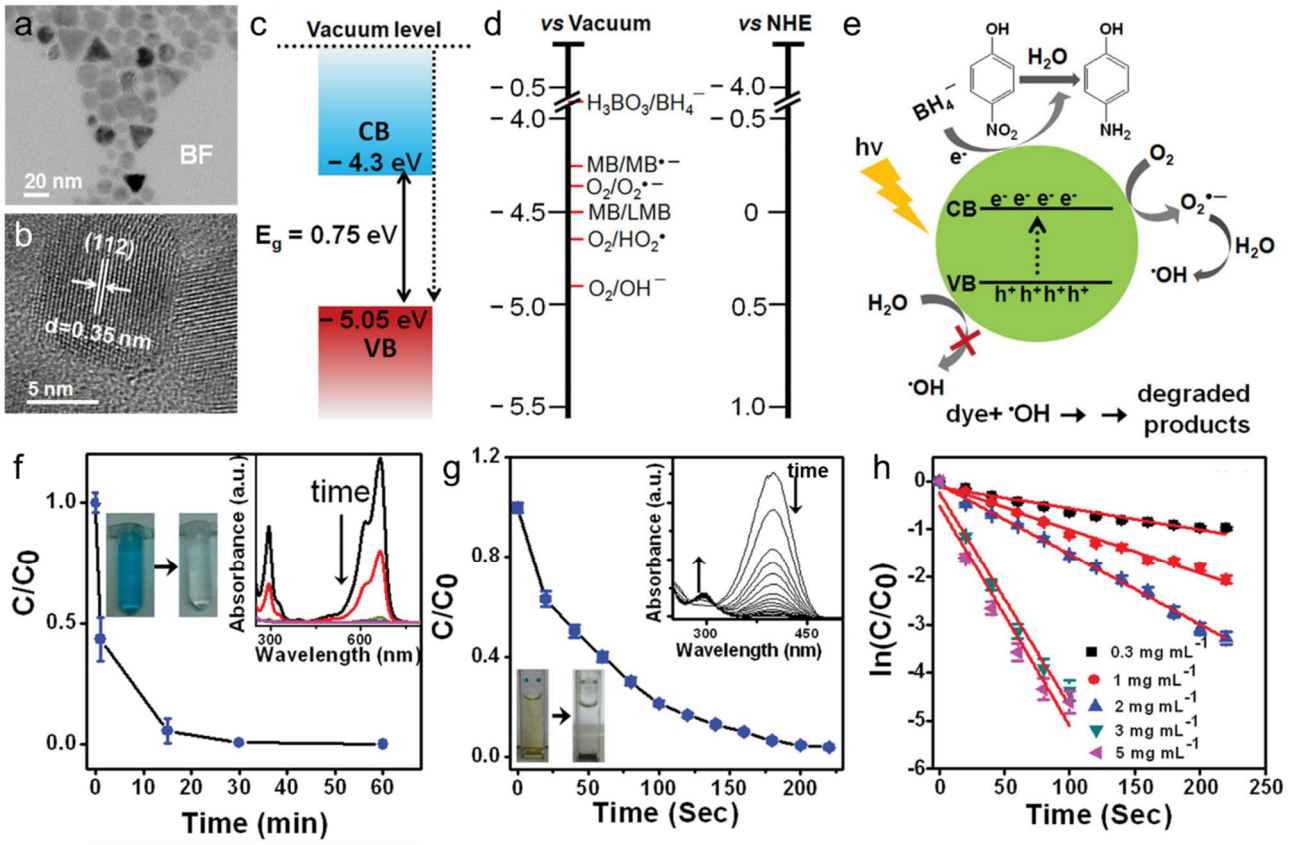

Figure 16. (**a**,**b**) TEM and HRTEM images of CZFS nanocrystals. (**c**) Energy bandgap alignment of CZFS nanocrystals. (**d**) Standard redox potentials (E_0) of different oxidative species. (**e**) A schematic of the catalytic pathways involved in degrading organic dyes and 4-NP by H-CZFS NCs. (**f**) Photocatalytic degradation of methylene blue solution by H-CZFS nanocrystals. (**g**,**h**) Catalytic performance of CZFS nanocrystals for reduction of 4-NP to 4-AP in the presence of NaBH. The insert in g is the time-dependent absorption spectra [247].

5. Conclusions and Outlook

CQSNs demonstrate remarkable photocatalytic performance, attributed to their suitable bandgap for visible light absorption, unique electronic states, tunable atomic structure, and exceptional optoelectronic properties. In conclusion, we provide a summary of recent progress in the design and development of CQSNs for photocatalytic applications. We initially present the solution-based synthesis of CQSNs with precise composition, shape, size and crystal phase control. Several strategies have been implemented to further enhance their photocatalytic performance, including surface engineering, elemental doping, cocatalyst loading, vacancy engineering, and interface engineering. Finally, various photocatalytic applications of CQSNs have been explored, including hydrogen production through both photocatalytic and PEC methods, CO_2 reduction, organic synthesis, and pollutant removal. Despite the enhanced photocatalytic performance of CQSN photocatalysts, they still have certain limitations compared to other types of photocatalysts. Therefore, there is potential for further advancements in the development of CQSN photocatalysts, along with a series of remaining challenges. Firstly, the PCE of current CQSNs is insufficient for feasible practical applications. It is expected to design and synthesize other favorable CQSNs with novel electronic properties or structural features. Also, it is desirable to design new modification approaches by borrowing from the optimizing strategies in other catalytic fields, such as strain engineering, polarization, and high-entropy structure. Besides, utilization of the structure-function relationship of photocatalysts in material design enables the highly efficient preparation of photocatalysts and facilitates the strategic integration of various advantageous factors in photocatalysis.

Subsequently, the optimization and integration of synthetic technologies hold promise for fabricating novel types of CQSN photocatalysts. The conventional synthetic methods, including colloidal methods and hydrothermal and solvothermal approaches, still possess inherent limitations in fabricating nanocrystal structures. For example, the incorporation of additives can introduce novel structural characteristics that impact photocatalytic processes. Therefore, further innovative synthetic approaches are required to enhance the efficiency of CQSN photocatalysts.

Lastly, there is still a lack of investigations on the photocatalytic mechanism of CQSNs. It is necessary to study the mechanisms of how the CQSN photocatalysts work in different photocatalytic reactions in detail via in situ

characterizations, such as Fourier transform infrared spectroscopy, Electron paramagnetic resonance spectroscopy, X-ray photoelectron spectroscopy, X-ray absorption fine structure, Raman spectroscopy, etc. The determination of the charge transfer mechanism in various semiconductor heterojunctions is essential for advancing research on photocatalytic reactions. There are few reports about the research on the photogenerated carrier dynamics of CQSNs. The energy band matching, novel Z-scheme, and p-n heterojunctions all fall under the category of traditional type-II heterojunctions; however, they exhibit distinct charge transfer mechanisms. It is highly useful to explore the photogenerated carrier separation and migration of CQSN photocatalysts via transient absorption spectroscopy, transient emission spectroscopy, optical pump THz probe spectroscopy and theoretical calculations. A thorough study of photogenerated carrier dynamics in CQSN photocatalysts can aid in the rational design of catalysts to achieve improved photocatalytic performance.

Author Contributions

B.Z., S.C., Q.J. and L.W. conceived the idea. L.W. wrote the paper. B.Z., S.C. and Q.J. revised the paper. All authors assisted during the manuscript preparation.

Ethics Statement

Not applicable.

Informed Consent Statement

Not applicable.

Funding

This research was funded by the National Natural Science Foundation of China (Grants 22101271, 22471005), the National Key Research and Development Program of China (Grants 2021YFA0715703).

Declaration of Competing Interest

The authors declare no competing interests.

References

1. Rahman MZ, Kibria MG, Mullins CB. Metal-free photocatalysts for hydrogen evolution. *Chem. Soc. Rev.* **2020**, *49*, 1887–1931.
2. Rahman MZ, Edvinsson T, Gascon J. Hole utilization in solar hydrogen production. *Nat. Rev. Chem.* **2022**, *6*, 243–258.
3. Lenton T, Rockström J, Gaffney O, Rahmstorf S, Richardson K, Steffen W, et al. Climate tipping points—Too risky to bet against. *Nature* **2019**, *575*, 592–595.
4. Nishiyama H, Yamada T, Nakabayashi M, Maehara Y, Yamaguchi M, Kuromiya Y, et al. Photocatalytic solar hydrogen production from water on a 100 m^2-scale. *Nature* **2021**, *598*, 304–307.
5. Takata T, Jiang J, Sakata Y, Nakabayashi M, Shibata N, Nandal V, et al. Photocatalytic water splitting with a quantum efficiency of almost unity. *Nature* **2020**, *581*, 411–414.
6. Zhou P, Navid IA, Ma Y, Xiao Y, Wang P, Ye Z, et al. Solar-to-hydrogen efficiency of more than 9% in photocatalytic water splitting. *Nature* **2023**, *613*, 66–70.
7. Jiang Z, Xu X, Ma Y, Cho HS, Ding D, Wang C, et al. Filling metal-organic framework mesopores with TiO_2 for CO_2 photoreduction. *Nature* **2020**, *586*, 549–554.
8. Li S, Liu C, Lv W, Liu G. Incorporating Oxygen Atoms in a SnS_2 Atomic Layer to Simultaneously Stabilize Atomic Hydrogen and Accelerate the Generation of Hydroxyl Radicals for Water Decontamination. *Environ. Sci. Technol.* **2022**, *56*, 4980–4987.
9. Li XD, Sun YF, Xu JQ, Shao YJ, Wu J, Xu XL, et al. Selective visible-light-driven photocatalytic CO_2 reduction to CH_4 mediated by atomically thin CuIn5S8 layers. *Nat. Energy* **2019**, *4*, 690–699.
10. Goto Y, Hisatomi T, Wang Q, Higashi T, Ishikiriyama K, Maeda T, et al. A Particulate Photocatalyst Water-Splitting Panel for Large-Scale Solar Hydrogen Generation. *Joule* **2018**, *2*, 509–520.
11. Li YY, Zhou H, Cai SH, Prabhakaran D, Niu WT, Large A, et al. Electrolyte-assisted polarization leading to enhanced charge separation and solar-to-hydrogen conversion efficiency of seawater splitting. *Nat. Catal.* **2024**, *7*, 77–88.
12. Kong T, Jiang Y, Xiong Y. Photocatalytic CO_2 conversion: What can we learn from conventional CO_x hydrogenation? *Chem. Soc. Rev.* **2020**, *49*, 6579–6591.

13. Bonchio M, Bonin J, Ishitani O, Lu T-B, Morikawa T, Morris AJ, et al. Best practices for experiments and reporting in photocatalytic CO_2 reduction. *Nat. Catal.* **2023**, *6*, 657–665.
14. Chen S, Takata T, Domen K. Particulate photocatalysts for overall water splitting. *Nat. Rev. Mater.* **2017**, *2*, 17050.
15. Chang K, Hai X, Ye JH. Transition Metal Disulfides as Noble-Metal-Alternative Co-Catalysts for Solar Hydrogen Production. *Adv. Energy Mater.* **2016**, *6*, 1502555.
16. Xiong J, Li H, Zhou J, Di J. Recent progress of indium-based photocatalysts: Classification, regulation and diversified applications. *Coord. Chem. Rev.* **2022**, *473*, 214819.
17. Wang Q, Pornrungroj C, Linley S, Reisner E. Strategies to improve light utilization in solar fuel synthesis. *Nat. Energy* **2022**, *7*, 13–24.
18. Meng XG, Liu LQ, Ouyang SX, Xu H, Wang DF, Zhao NQ, et al. Nanometals for Solar-to-Chemical Energy Conversion: From Semiconductor-Based Photocatalysis to Plasmon-Mediated Photocatalysis and Photo-Thermocatalysis. *Adv. Mater.* **2016**, *28*, 6781–6803.
19. Kosco J, Bidwell M, Cha H, Martin T, Howells CT, Sachs M, et al. Enhanced photocatalytic hydrogen evolution from organic semiconductor heterojunction nanoparticles. *Nat. Mater.* **2020**, *19*, 559–565.
20. Zhou P, Luo M, Guo S. Optimizing the semiconductor–metal-single-atom interaction for photocatalytic reactivity. *Nat. Rev. Chem.* **2022**, *6*, 823–838.
21. Fujishima A. Electrochemical photolysis of water at a semiconductor electrode. *Nature* **1972**, *238*, 37–38.
22. Chen X, Liu L, Yu PY, Mao SS. Increasing Solar Absorption for Photocatalysis with Black Hydrogenated Titanium Dioxide Nanocrystals. *Science* **2011**, *331*, 746–750.
23. Liu J, Liu Y, Liu N, Han Y, Zhang X, Huang H, et al. Metal-free efficient photocatalyst for stable visible water splitting via a two-electron pathway. *Science* **2015**, *347*, 970–974.
24. Su DW, Ran J, Zhuang ZW, Chen C, Qiao SZ, Li YD, et al. Atomically dispersed Ni in cadmium-zinc sulfide quantum dots for high-performance visible-light photocatalytic hydrogen production. *Sci. Adv.* **2020**, *6*, eaaz8447.
25. Zhou Q, Guo Y, Zhu Y. Photocatalytic sacrificial H_2 evolution dominated by micropore-confined exciton transfer in hydrogen-bonded organic frameworks. *Nat. Catal.* **2023**, *6*, 574–584.
26. Zhao D, Wang Y, Dong C-L, Huang Y-C, Chen J, Xue F, et al. Boron-doped nitrogen-deficient carbon nitride-based Z-scheme heterostructures for photocatalytic overall water splitting. *Nat. Energy* **2021**, *6*, 388–397.
27. Jiao X, Chen Z, Li X, Sun Y, Gao S, Yan W, et al. Defect-Mediated Electron–Hole Separation in One-Unit-Cell $ZnIn_2S_4$ Layers for Boosted Solar-Driven CO_2 Reduction. *J. Am. Chem. Soc.* **2017**, *139*, 7586–7594.
28. Li Y, Zhuang TT, Fan F, Voznyy O, Askerka M, Zhu H, et al. Pulsed axial epitaxy of colloidal quantum dots in nanowires enables facet-selective passivation. *Nat. Commun.* **2018**, *9*, 4947.
29. Han Z, Qiu F, Eisenberg R, Holland PL, Krauss TD. Robust Photogeneration of H_2 in Water Using Semiconductor Nanocrystals and a Nickel Catalyst. *Science* **2012**, *338*, 1321–1324.
30. Wang Z, Inoue Y, Hisatomi T, Ishikawa R, Wang Q, Takata T, et al. Overall water splitting by Ta_3N_5 nanorod single crystals grown on the edges of $KTaO_3$ particles. *Nat. Catal.* **2018**, *1*, 756–763.
31. Wang H, Qi H, Sun X, Jia S, Li X, Miao TJ, et al. High quantum efficiency of hydrogen production from methanol aqueous solution with PtCu–TiO_2 photocatalysts. *Nat. Mater.* **2023**, *22*, 619–626.
32. Wang Q, Nakabayashi M, Hisatomi T, Sun S, Akiyama S, Wang Z, et al. Oxysulfide photocatalyst for visible-light-driven overall water splitting. *Nat. Mater.* **2019**, *18*, 827–832.
33. Zhang Y, Li Y, Xin X, Wang Y, Guo P, Wang R, et al. Internal quantum efficiency higher than 100% achieved by combining doping and quantum effects for photocatalytic overall water splitting. *Nat. Energy* **2023**, *8*, 504–514.
34. Wang YO, Vogel A, Sachs M, Sprick RS, Wilbraham L, Moniz SJA, et al. Current understanding and challenges of solar-driven hydrogen generation using polymeric photocatalysts. *Nat. Energy* **2019**, *4*, 746–760.
35. Regulacio MD, Han MY. Multinary I-III-VI2 and I2-II-IV-VI4 Semiconductor Nanostructures for Photocatalytic Applications. *Acc. Chem. Res.* **2016**, *49*, 511–519.
36. Hu P, Pramana SS, Cao S, Ngaw CK, Lin J, Loo SCJ, et al. Ion-Induced Synthesis of Uniform Single-Crystalline Sulphide-Based Quaternary-Alloy Hexagonal Nanorings for Highly Efficient Photocatalytic Hydrogen Evolution. *Adv. Mater.* **2013**, *25*, 2567–2572.
37. Ha E, Lee LY, Wang J, Li F, Wong KY, Tsang SC. Significant enhancement in photocatalytic reduction of water to hydrogen by Au/Cu_2 $ZnSnS_4$ nanostructure. *Adv. Mater.* **2014**, *26*, 3496–3500.
38. Stroyuk O, Raevskaya A, Gaponik N. Solar light harvesting with multinary metal chalcogenide nanocrystals. *Chem. Soc. Rev.* **2018**, *47*, 5354–5422.
39. Yan C, Sun K, Huang J, Johnston S, Liu F, Veettil BP, et al. Beyond 11% Efficient Sulfide Kesterite $Cu_2Zn_xCd_{1-x}SnS_4$ Solar Cell: Effects of Cadmium Alloying. *ACS Energy Lett.* **2017**, *2*, 930–936.
40. Liu X-Y, Zhang G, Chen H, Li H, Jiang J, Long Y-T, et al. Efficient defect-controlled photocatalytic hydrogen generation based on near-infrared Cu-In-Zn-S quantum dots. *Nano Res.* **2017**, *11*, 1379–1388.

41. Tsuji I, Kato H, Kobayashi H, Kudo A. Photocatalytic H_2 Evolution under Visible-Light Irradiation over Band-Structure-Controlled $(CuIn)_xZn_{2(1-x)}S_2$ Solid Solutions. *J. Phys. Chem. B* **2005**, *109*, 7323–7329.
42. Tsuji I, Shimodaira Y, Kato H, Kobayashi H, Kudo A. Novel Stannite-type Complex Sulfide Photocatalysts AI2-Zn-AIV-S4 (AI = Cu and Ag; AIV = Sn and Ge) for Hydrogen Evolution under Visible-Light Irradiation. *Chem. Mater.* **2010**, *22*, 1402–1409.
43. Just J, Coughlan C, Singh S, Ren H, Muller O, Becker P, et al. Insights into Nucleation and Growth of Colloidal Quaternary Nanocrystals by Multimodal X-ray Analysis. *ACS Nano* **2021**, *15*, 6439–6447.
44. Tiong VT, Zhang Y, Bell J, Wang HX. Phase-selective hydrothermal synthesis of Cu_2ZnSnS_4 nanocrystals: The effect of the sulphur precursor. *CrystEngComm* **2014**, *16*, 4306–4313.
45. Xiao G, Ren X, Hu Y, Cao Y, Li Z, Shi Z, et al. Spin-Coated CZTS Film with a Gradient Cu-Deficient Interfacial Layer for Solar Hydrogen Evolution. *ACS Energy Lett.* **2024**, *9*, 715–726.
46. Zou C, Zhang L, Zhai L, Lin D, Gao J, Li Q, et al. Solution-based synthesis of quaternary Cu-In-Zn-S nanobelts with tunable composition and band gap. *Chem. Commun.* **2011**, *47*, 5256–5258.
47. Zhang W, Zhong X. Facile synthesis of ZnS-$CuInS_2$-alloyed nanocrystals for a color-tunable fluorchrome and photocatalyst. *Inorg. Chem.* **2011**, *50*, 4065–4072.
48. Xu M, Zai J, Yuan Y, Qian X. Band gap-tunable $(CuIn)_xZn_{2(1-x)}S_2$ solid solutions: Preparation and efficient photocatalytic hydrogen production from water under visible light without noble metals. *J. Mater. Chem.* **2012**, *22*, 23929.
49. Bora A, Lox J, Hübner R, Weiß N, Bahmani Jalali H, di Stasio F, et al. Composition-Dependent Optical Properties of Cu–Zn–In–Se Colloidal Nanocrystals Synthesized via Cation Exchange. *Chem. Mater.* **2023**, *35*, 4068–4077.
50. Chen S, Walsh A, Gong XG, Wei SH. Classification of lattice defects in the kesterite Cu_2ZnSnS_4 and $Cu_2ZnSnSe_4$ earth-abundant solar cell absorbers. *Adv. Mater.* **2013**, *25*, 1522–1539.
51. Liu Z, Fu H, Li Y, Liu J, Huang Y, Zhu D, et al. Composition-Engineered Heavy-Metal-Free Cu–Ga–Zn–S Nanorods for Efficient Photocatalytic Water Splitting. *ACS Appl. Nano Mater.* **2023**, *6*, 14401–14409.
52. Liu Q, Zhao Z, Lin Y, Guo P, Li S, Pan D, et al. Alloyed $(ZnS)_x(Cu_2SnS_3)_{1-x}$ and $(CuInS_2)_x(Cu_2SnS_3)_{1-x}$ nanocrystals with arbitrary composition and broad tunable band gaps. *Chem. Commun.* **2011**, *47*, 964–966.
53. Zhao J, Minegishi T, Kaneko H, Ma G, Zhong M, Nakabayashi M, et al. Efficient hydrogen evolution on $(CuInS_2)_x(ZnS)_{1-x}$ solid solution-based photocathodes under simulated sunlight. *Chem. Commun.* **2019**, *55*, 470–473.
54. Fan F-J, Wu L, Yu S-H. Energetic I–III–VI 2 and I 2–II–IV–VI 4 nanocrystals: Synthesis, photovoltaic and thermoelectric applications. *Energy Environ. Sci.* **2013**, *7*, 190–208.
55. Cai M, Tong X, Zhao H, Liao P, Pan L, Li G, et al. Regulating intragap states in colloidal quantum dots for universal photocatalytic hydrogen evolution. *Appl. Catal. B* **2024**, *343*, 123572.
56. Ye C, Regulacio MD, Lim SH, Xu QH, Han MY. Alloyed $(ZnS)_x(CuInS_2)_{(1-x)}$ semiconductor nanorods: Synthesis, bandgap tuning and photocatalytic properties. *Chem. Eur. J.* **2012**, *18*, 11258–11263.
57. Wu L, Wang Q, Zhuang T-T, Li Y, Zhang G, Liu G-Q, et al. Single crystalline quaternary sulfide nanobelts for efficient solar-to-hydrogen conversion. *Nat. Commun.* **2020**, *11*, 5194.
58. Chen Y, Qin Z, Guo X, Wang X, Guo L. One-step hydrothermal synthesis of $(CuIn)_{0.2}Zn_{1.6}S_2$ hollow sub-microspheres for efficient visible-light-driven photocatalytic hydrogen generation. *Int. J. Hydrogen Energy* **2016**, *41*, 1524–1534.
59. Liu B, Yang H, Liu S. Photogenerated Charge Separation between Polar Crystal Facets Under a Spontaneous Electric Field. *Adv. Optical Mater.* **2021**, *9*, 2001898.
60. Lin L, Lin Z, Zhang J, Cai X, Lin W, Yu Z, et al. Molecular-level insights on the reactive facet of carbon nitride single crystals photocatalysing overall water splitting. *Nat. Catal.* **2020**, *3*, 649–655.
61. Lin R, Wan J, Xiong Y, Wu K, Cheong WC, Zhou G, et al. Quantitative Study of Charge Carrier Dynamics in Well-Defined WO_3 Nanowires and Nanosheets: Insight into the Crystal Facet Effect in Photocatalysis. *J. Am. Chem. Soc.* **2018**, *140*, 9078–9082.
62. Zhang X, Guo G, Ji C, Huang K, Zha C, Wang Y, et al. Efficient Thermolysis Route to Monodisperse Cu_2ZnSnS_4 Nanocrystals with Controlled Shape and Structure. *Sci. Rep.* **2014**, *4*, 5086.
63. Shavel A, Ibanez M, Luo Z, De Roo J, Carrete A, Dimitrievska M, et al. Scalable Heating-Up Synthesis of Monodisperse Cu_2ZnSnS_4 Nanocrystals. *Chem. Mater.* **2016**, *28*, 720–726.
64. Singh A, Geaney H, Laffir F, Ryan KM. Colloidal Synthesis of Wurtzite Cu_2ZnSnS_4 Nanorods and Their Perpendicular Assembly. *J. Am. Chem. Soc.* **2012**, *134*, 2910–2913.
65. Zhou Y, Zhang Y, Lin M, Long J, Zhang Z, Lin H, et al. Monolayered Bi_2WO_6 nanosheets mimicking heterojunction interface with open surfaces for photocatalysis. *Nat. Commun.* **2015**, *6*, 8340.
66. Tian B, Tian B, Smith B, Scott MC, Lei Q, Hua R, et al. Facile bottom-up synthesis of partially oxidized black phosphorus nanosheets as metal-free photocatalyst for hydrogen evolution. *Proc. Natl. Acad. Sci. USA* **2018**, *115*, 4345–4350.
67. Sun X, Luo X, Jin S, Zhang X, Wang H, Shao W, et al. Surface modification of $ZnIn_2S_4$ layers to realise energy transfer-mediated photocatalysis. *Natl. Sci. Rev.* **2022**, *9*, nwac026.

68. Zhang X, Xu Y, Zhang J, Dong S, Shen L, Gupta A, et al. Synthesis of Wurtzite Cu_2ZnSnS_4 Nanosheets with Exposed High-Energy (002) Facets for Fabrication of Efficient Pt-Free Solar Cell Counter Electrodes. *Sci. Rep.* **2018**, *8*, 248.
69. Wang Y, Zhang Y, Xin X, Yang J, Wang M, Wang R, et al. In situ photocatalytically enhanced thermogalvanic cells for electricity and hydrogen production. *Science* **2023**, *381*, 291–296.
70. Yang J, Hou Y, Sun J, Wei J, Zhang S, Liang J, et al. Corn-straw-derived, pyridine-nitrogen-rich NCQDs modified $Cu_{0.05}Zn_{2.95}In_2S_6$ promoted directional electrons transfer and boosted adsorption and activation of CO_2 for efficient photocatalytic reduction of CO_2 to CO. *Chem. Eng. J.* **2023**, *472*, 145142.
71. Qiu B, Zhu Q, Du M, Fan L, Xing M, Zhang J. Efficient Solar Light Harvesting CdS/Co_9S_8 Hollow Cubes for Z-Scheme Photocatalytic Water Splitting. *Angew. Chem. Int. Ed.* **2017**, *56*, 2684–2688.
72. Sun Y, Hu Z, Zhang J, Wang L, Wu C, Xu J. A top-down strategy to synthesize wurtzite Cu_2ZnSnS_4 nanocrystals by green chemistry. *Chem. Commun.* **2016**, *52*, 9821–9824.
73. Dong C, Lian C, Hu S, Deng Z, Gong J, Li M, et al. Size-dependent activity and selectivity of carbon dioxide photocatalytic reduction over platinum nanoparticles. *Nat. Commun.* **2018**, *9*, 1252.
74. Fan YY, Zhou WC, Qiu XY, Li HD, Jiang YH, Sun ZH, et al. Selective photocatalytic oxidation of methane by quantum-sized bismuth vanadate. *Nat. Sustain.* **2021**, *4*, 509–515.
75. Xia C, Wu W, Yu T, Xie X, van Oversteeg C, Gerritsen HC, et al. Size-Dependent Band-Gap and Molar Absorption Coefficients of Colloidal $CuInS_2$ Quantum Dots. *ACS Nano* **2018**, *12*, 8350–8361.
76. Chen X, Shen S, Guo L, Mao SS. Semiconductor-based Photocatalytic Hydrogen Generation. *Chem. Rev.* **2010**, *110*, 6503–6570.
77. Qi M-Y, Conte M, Anpo M, Tang Z-R, Xu Y-J. Cooperative Coupling of Oxidative Organic Synthesis and Hydrogen Production over Semiconductor-Based Photocatalysts. *Chem. Rev.* **2021**, *121*, 13051–13085.
78. Jara DH, Yoon SJ, Stamplecoskie KG, Kamat PV. Size-Dependent Photovoltaic Performance of $CuInS_2$Quantum Dot-Sensitized Solar Cells. *Chem. Mater.* **2014**, *26*, 7221–7228.
79. Chen X, Ge J, Xiao P, Deng Y, Wang Y. Ligand-induced, magic-size clusters enabled formation of colloidal all-inorganic II–VI nanoplatelets with controllable lateral dimensions. *Nano Res.* **2022**, *16*, 3387–3394.
80. Zhang J, Xie R, Yang W. A Simple Route for Highly Luminescent Quaternary Cu-Zn-In-S Nanocrystal Emitters. *Chem. Mater.* **2011**, *23*, 3357–3361.
81. Nishi H, Nagano T, Kuwabata S, Torimoto T. Controllable electronic energy structure of size-controlled Cu_2ZnSnS_4 nanoparticles prepared by a solution-based approach. *PCCP* **2014**, *16*, 672–675.
82. Chang ZX, Zhou WH, Kou DX, Zhou ZJ, Wu SX. Phase-dependent photocatalytic H_2 evolution of copper zinc tin sulfide under visible light. *Chem. Commun.* **2014**, *50*, 12726–12729.
83. Wang W, Wang Z, Yang R, Duan J, Liu Y, Nie A, et al. In Situ Phase Separation into Coupled Interfaces for Promoting CO_2 Electroreduction to Formate over a Wide Potential Window. *Angew. Chem. Int. Ed.* **2021**, *60*, 22940–22947.
84. Wang J, Chen Y, Zhou W, Tian G, Xiao Y, Fu H, et al. Cubic quantum dot/hexagonal microsphere $ZnIn_2S_4$ heterophase junctions for exceptional visible-light-driven photocatalytic H_2 evolution. *J. Mater. Chem. A* **2017**, *5*, 8451–8460.
85. Kreft S, Wei D, Junge H, Beller M. Recent advances on TiO_2-based photocatalytic CO_2 reduction. *EnergyChem* **2020**, *2*, 100044.
86. Chen SY, Walsh A, Luo Y, Yang JH, Gong XG, Wei SH. Wurtzite-derived polytypes of kesterite and stannite quaternary chalcogenide semiconductors. *Phys. Rev. B* **2010**, *82*, 195203.
87. Chen SY, Gong XG, Walsh A, Wei SH. Electronic structure and stability of quaternary chalcogenide semiconductors derived from cation cross-substitution of II-VI and I-III-VI(2) compounds. *Phys. Rev. B* **2009**, *79*, 165211.
88. Zhao Z, Ma C, Cao Y, Yi J, He X, Qiu J. Electronic structure and optical properties of wurtzite-kesterite Cu_2ZnSnS_4. *Phys. Lett. A* **2013**, *377*, 417–422.
89. Pan D, An L, Sun Z, Hou W, Yang Y, Yang Z, et al. Synthesis of Cu−In−S ternary nanocrystals with tunable structure and composition. *J. Am. Chem. Soc.* **2008**, *130*, 5620–5621.
90. Kamble A, Sinha B, Vanalakar S, Agawane G, Gang MG, Kim JY, et al. Monodispersed wurtzite Cu_2SnS_3nanocrystals by phosphine and oleylamine free facile heat-up technique. *CrystEngComm* **2016**, *18*, 2885–2893.
91. Huang S, Zai J, Ma D, He Q, Liu Y, Qiao Q, et al. Colloidal synthesis of wurtz-stannite Cu_2CdGeS_4 nanocrystals with high catalytic activity toward iodine redox couples in dye-sensitized solar cells. *Chem. Commun.* **2016**, *52*, 10866–10869.
92. Lu X, Zhuang Z, Peng Q, Li Y. Wurtzite Cu_2ZnSnS_4 nanocrystals: A novel quaternary semiconductor. *Chem. Commun.* **2011**, *47*, 3141–3143.
93. Li Z, Lui ALK, Lam KH, Xi L, Lam YM. Phase-Selective Synthesis of Cu_2ZnSnS_4 Nanocrystals using Different Sulfur Precursors. *Inorg. Chem.* **2014**, *53*, 10874–10880.
94. Batabyal SK, Tian L, Venkatram N, Ji W, Vittal JJ. Phase-selective synthesis of $CuInS_2$ nanocrystals. *J. Phys. Chem. C* **2009**, *113*, 15037–15042.
95. Wang YX, Wei M, Fan FJ, Zhuang TT, Wu L, Yu SH, et al. Phase-Selective Synthesis of Cu_2ZnSnS_4 Nanocrystals through Cation Exchange for Photovoltaic Devices. *Chem. Mater.* **2014**, *26*, 5492–5498.

96. Zou Y, Su X, Jiang J. Phase-controlled synthesis of Cu_2ZnSnS_4 nanocrystals: The role of reactivity between Zn and S. *J. Am. Chem. Soc.* **2013**, *135*, 18377–18384.
97. Zhang Y, Han L, Wang C, Wang W, Ling T, Yang J, et al. Zinc-Blende CdS Nanocubes with Coordinated Facets for Photocatalytic Water Splitting. *ACS Catal.* **2017**, *7*, 1470–1477.
98. Jiang WC, Ni CW, Zhang LC, Shi M, Qu JS, Zhou HP, et al. Tuning the Anisotropic Facet of Lead Chromate Photocatalysts to Promote Spatial Charge Separation. *Angew. Chem. Int. Ed.* **2022**, *61*, e20220716.
99. Shi M, Li G, Li J, Jin X, Tao X, Zeng B, et al. Intrinsic Facet-Dependent Reactivity of Well-Defined BiOBr Nanosheets on Photocatalytic Water Splitting. *Angew. Chem. Int. Ed.* **2020**, *59*, 6590–6595.
100. Zhang W, Yang Z, Wang H, Lu L, Liu D, Li T, et al. Crystal facet-dependent frustrated Lewis pairs on dual-metal hydroxide for photocatalytic CO_2 reduction. *Appl. Catal. B* **2022**, *300*, 120748.
101. Bi Y, Ouyang S, Umezawa N, Cao J, Ye J. Facet Effect of Single-Crystalline Ag_3PO_4 Sub-microcrystals on Photocatalytic Properties. *J. Am. Chem. Soc.* **2011**, *133*, 6490–6492.
102. Ke J, Zhao J, Chi M, Wang M, Kong X, Chang Q, et al. Facet-dependent electrooxidation of propylene into propylene oxide over Ag_3PO_4 crystals. *Nat. Commun.* **2022**, *13*, 932.
103. Dang Y, Luo L, Wang W, Hu W, Wen X, Lin K, et al. Improving the Photocatalytic H_2 Evolution of CdS by Adjusting the (002) Crystal Facet. *J. Phys. Chem. C* **2022**, *126*, 1346–1355.
104. Wang X, Liu M, Zhou Z, Guo L. Toward Facet Engineering of CdS Nanocrystals and Their Shape-Dependent Photocatalytic Activities. *J. Phys. Chem. C* **2015**, *119*, 20555–20560.
105. Yu J, Low J, Xiao W, Zhou P, Jaroniec M. Enhanced Photocatalytic CO_2-Reduction Activity of Anatase TiO_2 by Coexposed {001} and {101} Facets. *J. Am. Chem. Soc.* **2014**, *136*, 8839–8842.
106. Xiong J, Song P, Di J, Li H. Ultrathin structured photocatalysts: A versatile platform for CO_2 reduction. *Appl. Catal. B* **2019**, *256*, 117788.
107. Yang J, Zeng X, Tebyetekerwa M, Wang Z, Bie C, Sun X, et al. Engineering 2D Photocatalysts for Solar Hydrogen Peroxide Production. *Adv. Energy Mater.* **2024**, *14*, 2400740.
108. Shi X, Dai C, Wang X, Hu J, Zhang J, Zheng L, et al. Protruding Pt single-sites on hexagonal $ZnIn_2S_4$ to accelerate photocatalytic hydrogen evolution. *Nat. Commun.* **2022**, *13*, 1287.
109. Xiao JD, Nishimae S, Vequizo JJM, Nakabayashi M, Hisatomi T, Li HH, et al. Enhanced Overall Water Splitting by a Zirconium-Doped TaON-Based Photocatalyst. *Angew. Chem. Int. Ed.* **2022**, *61*, e202116573.
110. Liu Y, Zhou Y, Zhou X, Jin X, Li B, Liu J, et al. Cu doped SnS_2 nanostructure induced sulfur vacancy towards boosted photocatalytic hydrogen evolution. *Chem. Eng. J.* **2021**, *407*, 127180.
111. Zhou DX, Xue XD, Wang X, Luan QJ, Li A, Zhang LG, et al. Ni, In co-doped $ZnIn_2S_4$ for efficient hydrogen evolution: Modulating charge flow and balancing H adsorption/desorption. *Appl. Catal. B.* **2022**, *310*, 121337.
112. Li MM, Zhang H, Zhao ZY, Wang PF, Li Y, Zhan SH. Inorganic Ultrathin 2D Photocatalysts: Modulation Strategies and Environmental/Energy Applications. *Acc. Mater. Res.* **2023**, *4*, 4–15.
113. Li XG, Bi WT, Zhang L, Tao S, Chu WS, Zhang Q, et al. Single-Atom Pt as Co-Catalyst for Enhanced Photocatalytic H_2 Evolution. *Adv. Mater.* **2016**, *28*, 2427–2431.
114. Wang P, Shen Z, Xia Y, Wang H, Zheng L, Xi W, et al. Atomic Insights for Optimum and Excess Doping in Photocatalysis: A Case Study of Few-Layer Cu-$ZnIn_2S_4$. *Adv. Funct. Mater.* **2019**, *29*, 1807013.
115. Huang C, Chen C, Zhang M, Lin L, Ye X, Lin S, et al. Carbon-doped BN nanosheets for metal-free photoredox catalysis. *Nat. Commun.* **2015**, *6*, 7698.
116. Jiao X, Li X, Jin X, Sun Y, Xu J, Liang L, et al. Partially Oxidized SnS_2 Atomic Layers Achieving Efficient Visible-Light-Driven CO_2 Reduction. *J. Am. Chem. Soc.* **2017**, *139*, 18044–18051.
117. Shi R, Ye HF, Liang F, Wang Z, Li K, Weng Y, et al. Interstitial P-Doped CdS with Long-Lived Photogenerated Electrons for Photocatalytic Water Splitting without Sacrificial Agents. *Adv. Mater.* **2018**, *30*, 1705941.
118. Shown I, Samireddi S, Chang Y-C, Putikam R, Chang P-H, Sabbah A, et al. Carbon-doped SnS_2 nanostructure as a high-efficiency solar fuel catalyst under visible light. *Nat. Commun.* **2018**, *9*, 169.
119. Wu L, Su F, Liu T, Liu G-Q, Li Y, Ma T, et al. Phosphorus-Doped Single-Crystalline Quaternary Sulfide Nanobelts Enable Efficient Visible-Light Photocatalytic Hydrogen Evolution. *J. Am. Chem. Soc.* **2022**, *144*, 20620–20629.
120. Wang Q, Warnan J, Rodríguez-Jiménez S, Leung JJ, Kalathil S, Andrei V, et al. Molecularly engineered photocatalyst sheet for scalable solar formate production from carbon dioxide and water. *Nat. Energy* **2020**, *5*, 703–710.
121. Wang X, Wang X, Huang J, Li S, Meng A, Li Z. Interfacial chemical bond and internal electric field modulated Z-scheme Sv-$ZnIn_2S_4$/$MoSe_2$ photocatalyst for efficient hydrogen evolution. *Nat. Commun.* **2021**, *12*, 4112.
122. Bie C, Cheng B, Fan J, Ho W, Yu J. Enhanced solar-to-chemical energy conversion of graphitic carbon nitride by two-dimensional cocatalysts. *EnergyChem* **2021**, *3*, 100051.
123. Yang J, Wang D, Han H, Li C. Roles of cocatalysts in photocatalysis and photoelectrocatalysis. *Acc. Chem. Res.* **2013**, *46*, 1900–1909.

124. Ran J, Zhang J, Yu J, Jaroniec M, Qiao SZ. Earth-abundant cocatalysts for semiconductor-based photocatalytic water splitting. *Chem. Soc. Rev.* **2014**, *43*, 7787–7812.
125. Gao DD, Xu JC, Wang LX, Zhu BC, Yu HG, Yu JG. Optimizing Atomic Hydrogen Desorption of Sulfur-Rich NiS_{1+x} Cocatalyst for Boosting Photocatalytic H_2 Evolution. *Adv. Mater.* **2022**, *34*, 2108475.
126. Zhang H, Zhang P, Qiu M, Dong J, Zhang Y, Lou XW. Ultrasmall MoO_x Clusters as a Novel Cocatalyst for Photocatalytic Hydrogen Evolution. *Adv. Mater.* **2018**, *31*, 1804883.
127. Liu Y, Yang W, Chen Q, Cullen DA, Xie Z, Lian T. Pt Particle Size Affects Both the Charge Separation and Water Reduction Efficiencies of CdS–Pt Nanorod Photocatalysts for Light Driven H_2 Generation. *J. Am. Chem. Soc.* **2022**, *144*, 2705–2715.
128. Chang K, Mei Z, Wang T, Kang Q, Ouyang S, Ye J. MoS_2/Graphene Cocatalyst for Efficient Photocatalytic H_2 Evolution under Visible Light Irradiation. *ACS Nano* **2014**, *8*, 7078–7087.
129. Yue Q, Wan Y, Sun Z, Wu X, Yuan Y, Du P. MoP is a novel, noble-metal-free cocatalyst for enhanced photocatalytic hydrogen production from water under visible light. *J. Mater. Chem. A* **2015**, *3*, 16941–16947.
130. Wang Z, Luo Y, Hisatomi T, Vequizo JJM, Suzuki S, Chen S, et al. Sequential cocatalyst decoration on $BaTaO_2N$ towards highly-active Z-scheme water splitting. *Nat. Commun.* **2021**, *12*, 1005.
131. Dilsaver PS, Reichert MD, Hallmark BL, Thompson MJ, Vela J. Cu_2ZnSnS_4–Au Heterostructures: Toward Greener Chalcogenide-Based Photocatalysts. *J. Phys. Chem. C* **2014**, *118*, 21226–21234.
132. Yu X, An X, Genç A, Ibáñez M, Arbiol J, Zhang Y, et al. Cu_2ZnSnS_4–PtM (M = Co, Ni) Nanoheterostructures for Photocatalytic Hydrogen Evolution. *J. Phys. Chem. C* **2015**, *119*, 21882–21888.
133. Lin T, Yang T, Cai Y, Li J, Lu G, Chen S, et al. Transformation-Optics-Designed Plasmonic Singularities for Efficient Photocatalytic Hydrogen Evolution at Metal/Semiconductor Interfaces. *Nano Lett.* **2023**, *23*, 5288–5296.
134. Ye C, Regulacio MD, Lim SH, Li S, Xu QH, Han MY. Alloyed ZnS-$CuInS_2$ Semiconductor Nanorods and Their Nanoscale Heterostructures for Visible-Light-Driven Photocatalytic Hydrogen Generation. *Chem. Eur. J.* **2015**, *21*, 9514–9519.
135. Yu X, Shavel A, An X, Luo Z, Ibanez M, Cabot A. Cu_2ZnSnS_4-Pt and Cu_2ZnSnS_4-Au heterostructured nanoparticles for photocatalytic water splitting and pollutant degradation. *J. Am. Chem. Soc.* **2014**, *136*, 9236–9239.
136. Ha E, Liu W, Wang L, Man H-W, Hu L, Tsang SCE, et al. Cu_2ZnSnS_4/MoS_2-Reduced Graphene Oxide Heterostructure: Nanoscale Interfacial Contact and Enhanced Photocatalytic Hydrogen Generation. *Sci. Rep.* **2017**, *7*, 39411.
137. Li YL, Zhou ZH, Lin YL, Ji HN, Li HD, Wu J, et al. Significant Enhancement of Hydrogen Production in MoS_2/Cu_2ZnSnS_4 Nanoparticles. *Part. Part. Syst. Char.* **2018**, *35*, 1700472.
138. He Y, Chen C, Liu Y, Yang Y, Li C, Shi Z, et al. Quantitative Evaluation of Carrier Dynamics in Full-Spectrum Responsive Metallic $ZnIn_2S_4$ with Indium Vacancies for Boosting Photocatalytic CO_2 Reduction. *Nano Lett.* **2022**, *22*, 4970–4978.
139. He J, Hu L, Shao C, Jiang S, Sun C, Song S. Photocatalytic H_2O Overall Splitting into H_2 Bubbles by Single Atomic Sulfur Vacancy CdS with Spin Polarization Electric Field. *ACS Nano* **2021**, *15*, 18006–18013.
140. Wang Z, Xiao M, You J, Liu G, Wang L. Defect Engineering in Photocatalysts and Photoelectrodes: From Small to Big. *Acc. Mater. Res.* **2022**, *3*, 1127–1136.
141. Sun X, Zhang X, Xie Y. Surface Defects in Two-Dimensional Photocatalysts for Efficient Organic Synthesis. *Matter* **2020**, *2*, 842–861.
142. Fujiwara H, Hosokawa H, Murakoshi K, Wada Y, Yanagida S. Surface Characteristics of ZnS Nanocrystallites Relating to Their Photocatalysis for CO_2 Reduction1. *Langmuir* **1998**, *14*, 5154–5159.
143. Chen MX, Liu Y, Li CC, Li A, Chang XX, Liu W, et al. Spatial control of cocatalysts and elimination of interfacial defects towards efficient and robust CIGS photocathodes for solar water splitting. *Energy Environ. Sci.* **2018**, *11*, 2025–2034.
144. Niu Z, Gao X, Lou S, Wen N, Zhao J, Zhang Z, et al. Theory-Guided S-Defects Boost Selective Conversion of CO_2 to HCOOH over In4SnS8 Nanoflowers. *ACS Catal.* **2023**, *13*, 2998–3006.
145. Peng H, Yang H, Han J, Liu X, Su D, Yang T, et al. Defective $ZnIn_2S_4$ Nanosheets for Visible-Light and Sacrificial-Agent-Free H_2O_2 Photosynthesis via O_2/H_2O Redox. *J. Am. Chem. Soc.* **2023**, *145*, 27757–27766.
146. Chen S, Yang J-H, Gong XG, Walsh A, Wei S-H. Intrinsic point defects and complexes in the quaternary kesterite semiconductor Cu_2ZnSnS_4. *Phys. Rev. B* **2010**, *81*, 245204.
147. Nagoya A, Asahi R, Wahl R, Kresse G. Defect formation and phase stability of Cu_2ZnSnS_4 photovoltaic material. *Phys. Rev. B* **2010**, *81*, 113202.
148. Kumar M, Dubey A, Adhikari N, Venkatesan S, Qiao Q. Strategic review of secondary phases, defects and defect-complexes in kesterite CZTS-Se solar cells. *Energy Environ. Sci.* **2015**, *8*, 3134–3159.
149. Di J, Xia J, Chisholm MF, Zhong J, Chen C, Cao X, et al. Defect-Tailoring Mediated Electron–Hole Separation in Single-Unit-Cell Bi_3O_4Br Nanosheets for Boosting Photocatalytic Hydrogen Evolution and Nitrogen Fixation. *Adv. Mater.* **2019**, *31*, 1807576.
150. Xiong J, Di J, Xia J, Zhu W, Li H. Surface Defect Engineering in 2D Nanomaterials for Photocatalysis. *Adv. Funct. Mater.* **2018**, *28*, 1801983.
151. Li J, Huang Y, Huang J, Liang G, Zhang Y, Rey G, et al. Defect Control for 12.5% Efficiency Cu_2 $ZnSnSe_4$ Kesterite Thin-Film Solar Cells by Engineering of Local Chemical Environment. *Adv. Mater.* **2020**, *32*, e2005268.

152. Zhou H, Song TB, Hsu WC, Luo S, Ye S, Duan HS, et al. Rational Defect Passivation of $Cu_2ZnSn(S,Se)_4$ Photovoltaics with Solution-Processed Cu_2ZnSnS_4:Na Nanocrystals. *J. Am. Chem. Soc.* **2013**, *135*, 15998–16001.
153. Hansen EC, Liu Y, Utzat H, Bertram SN, Grossman JC, Bawendi MG. Blue Light Emitting Defective Nanocrystals Composed of Earth-Abundant Elements. *Angew. Chem. Int. Ed.* **2020**, *59*, 860–867.
154. Ortiz BR, Peng W, Gomes LC, Gorai P, Zhu T, Smiadak DM, et al. Ultralow Thermal Conductivity in Diamond-Like Semiconductors: Selective Scattering of Phonons from Antisite Defects. *Chem. Mater.* **2018**, *30*, 3395–3409.
155. Cai M, Tong X, Liao P, Shen S, Zhao H, Li X, et al. Manipulating the Optically Active Defect–Defect Interaction of Colloidal Quantum Dots for Carbon Dioxide Photoreduction. *ACS Catal.* **2023**, *13*, 15546–15557.
156. Ruan X, Meng D, Huang C, Xu M, Jiao D, Cheng H, et al. Artificial Photosynthetic System with Spatial Dual Reduction Site Enabling Enhanced Solar Hydrogen Production. *Adv. Mater.* **2024**, *36*, 2309199.
157. Lian Z, Wu F, Zi J, Li G, Wang W, Li H. Infrared Light-Induced Anomalous Defect-Mediated Plasmonic Hot Electron Transfer for Enhanced Photocatalytic Hydrogen Evolution. *J. Am. Chem. Soc.* **2023**, *145*, 15482–15487.
158. Chen Y, Zhao S, Wang X, Peng Q, Lin R, Wang Y, et al. Synergetic Integration of $Cu_{1.94}S$-$Zn_xCd_{1-x}S$ Heteronanorods for Enhanced Visible-Light-Driven Photocatalytic Hydrogen Production. *J. Am. Chem. Soc.* **2016**, *138*, 4286–4289.
159. Ruan XW, Huang CX, Cheng H, Zhang ZQ, Cui Y, Li ZY, et al. A Twin S-Scheme Artificial Photosynthetic System with Self-Assembled Heterojunctions Yields Superior Photocatalytic Hydrogen Evolution Rate. *Adv. Mater.* **2023**, *35*, 2209141.
160. Eshet H, Baer R, Neuhauser D, Rabani E. Theory of highly efficient multiexciton generation in type-II nanorods. *Nat. Commun.* **2016**, *7*, 13178.
161. McDaniel H, Pelton M, Oh N, Shim M. Effects of Lattice Strain and Band Offset on Electron Transfer Rates in Type-II Nanorod Heterostructures. *J Phys. Chem. Lett.* **2012**, *3*, 1094–1098.
162. Xu B, He P, Liu H, Wang P, Zhou G, Wang X. A 1D/2D Helical CdS/$ZnIn_2S_4$ Nano-Heterostructure. *Angew. Chem. Int. Ed.* **2014**, *53*, 2339–2343.
163. Gao C, Wang J, Xu HX, Xiong YJ. Coordination chemistry in the design of heterogeneous photocatalysts. *Chem. Soc. Rev.* **2017**, *46*, 2799–2823.
164. Garg P, Bhauriyal P, Mahata A, Rawat KS, Pathak B. Role of Dimensionality for Photocatalytic Water Splitting: CdS Nanotube versus Bulk Structure. *ChemPhysChem* **2019**, *20*, 383–391.
165. Zhuang TT, Liu Y, Sun M, Jiang SL, Zhang MW, Wang XC, et al. A Unique Ternary Semiconductor-(Semiconductor/Metal) Nano-Architecture for Efficient Photocatalytic Hydrogen Evolution. *Angew. Chem. Int. Ed.* **2015**, *54*, 11495–11500.
166. Yuan YP, Ruan LW, Barber J, Loo SCJ, Xue C. Hetero-nanostructured suspended photocatalysts for solar-to-fuel conversion. *Energy Environ. Sci.* **2014**, *7*, 3934–3951.
167. Low J, Yu J, Jaroniec M, Wageh S, Al-Ghamdi AA. Heterojunction Photocatalysts. *Adv. Mater.* **2017**, *29*, 1601694.
168. Jiang F, Pan B, You D, Zhou Y, Wang X, Su W. Visible light photocatalytic H_2-production activity of epitaxial Cu_2ZnSnS_4/ZnS heterojunction. *Catal. Commun.* **2016**, *85*, 39–43.
169. Choi Y, Beak M, Zhang Z, Dao V-D, Choi H-S, Yong K. Two-storey structure photoanode of 3D Cu_2ZnSnS_4/CdS/ZnO@steel composite nanostructure for efficient photoelectrochemical hydrogen generation. *Nanoscale* **2015**, *7*, 15291–15299.
170. Yuan M, Wang JL, Zhou WH, Chang ZX, Kou DX, Zhou ZJ, et al. Cu_2ZnSnS_4-CdS heterostructured nanocrystals for enhanced photocatalytic hydrogen production. *Catal. Sci. Technol.* **2017**, *7*, 3980–3984.
171. Yuan M, Zhou W-H, Kou D-X, Zhou Z-J, Meng Y-N, Wu S-X. Cu_2ZnSnS_4 decorated CdS nanorods for enhanced visible-light-driven photocatalytic hydrogen production. *Int. J. Hydrogen Energy* **2018**, *43*, 20408–20416.
172. Liu M, Jing D, Zhou Z, Guo L. Twin-induced one-dimensional homojunctions yield high quantum efficiency for solar hydrogen generation. *Nat. Commun.* **2013**, *4*, 2278.
173. Guan XJ, Zong SC, Shen SH. Homojunction photocatalysts for water splitting. *Nano Res.* **2022**, *15*, 10171–10184.
174. Wang J, Zhang YQ, Jiang SJ, Sun CZ, Song SQ. Regulation of d-Band Centers in Localized CdS Homojunctions through Facet Control for Improved Photocatalytic Water Splitting. *Angew. Chem. Int. Ed.* **2023**, *62*, e202307808.
175. Wang L, Sun Y, Zhang F, Hu J, Hu W, Xie S, et al. Precisely Constructed Metal Sulfides with Localized Single-Atom Rhodium for Photocatalytic C−H Activation and Direct Methanol Coupling to Ethylene Glycol. *Adv. Mater.* **2022**, *35*, 2205782.
176. Yeh C-Y, Lu Z, Froyen S, Zunger A. Zinc-blende–wurtzite polytypism in semiconductors. *Phys. Rev. B* **1992**, *46*, 10086–10097.
177. Singh S, Liu P, Singh A, Coughlan C, Wang JJ, Lusi M, et al. Colloidal $Cu_2ZnSn(SSe)_4$ (CZTSSe) Nanocrystals: Shape and Crystal Phase Control to Form Dots, Arrows, Ellipsoids, and Rods. *Chem. Mater.* **2015**, *27*, 4742–4748.
178. Ning JJ, Kershaw SV, Rogach AL. Synthesis and Optical Properties of Cubic Chalcopyrite/Hexagonal Wurtzite Core/Shell Copper Indium Sulfide Nanocrystals. *J. Am. Chem. Soc.* **2019**, *141*, 20516–20524.
179. Wang JJ, Liu P, Seaton CC, Ryan KM. Complete colloidal synthesis of Cu_2SnSe_3 nanocrystals with crystal phase and shape control. *J. Am. Chem. Soc.* **2014**, *136*, 7954–7960.
180. Wu L, Chen S-Y, Fan F-J, Zhuang T-T, Dai C-M, Yu S-H. Polytypic Nanocrystals of Cu-Based Ternary Chalcogenides: Colloidal Synthesis and Photoelectrochemical Properties. *J. Am. Chem. Soc.* **2016**, *138*, 5576–5584.

181. Wu L, Fan F-J, Gong M, Ge J, Yu S-H. Selective epitaxial growth of zinc blende-derivative on wurtzite-derivative: The case of polytypic $Cu_2CdSn(S_{1-x}Se_x)_4$ nanocrystals. *Nanoscale* **2014**, *6*, 3418–3422.
182. Wu L, Wang Q, Zhuang T-T, Zhang G-Z, Li Y, Li H-H, et al. A library of polytypic copper-based quaternary sulfide nanocrystals enables efficient solar-to-hydrogen conversion. *Nat. Commun.* **2022**, *13*, 5414.
183. Yang R, Mei L, Fan Y, Zhang Q, Zhu R, Amal R, et al. $ZnIn_2S_4$-Based Photocatalysts for Energy and Environmental Applications. *Small Methods* **2021**, *5*, 2100887.
184. Fu CF, Wu X, Yang J. Material Design for Photocatalytic Water Splitting from a Theoretical Perspective. *Adv. Mater.* **2018**, *30*, e1802106.
185. Li X-B, Tung C-H, Wu L-Z. Semiconducting quantum dots for artificial photosynthesis. *Nat. Rev. Chem.* **2018**, *2*, 160–173.
186. Miao YX, Zhao YX, Zhang S, Shi R, Zhang TR. Strain Engineering: A Boosting Strategy for Photocatalysis. *Adv. Mater.* **2022**, *34*, 2200868.
187. Wang YO, Suzuki H, Xie JJ, Tomita O, Martin DJ, Higashi M, et al. Mimicking Natural Photosynthesis: Solar to Renewable H_2 Fuel Synthesis by Z-Scheme Water Splitting Systems. *Chem. Rev.* **2018**, *118*, 5201–5241.
188. Wang Z, Hisatomi T, Li R, Sayama K, Liu G, Domen K, et al. Efficiency Accreditation and Testing Protocols for Particulate Photocatalysts toward Solar Fuel Production. *Joule* **2021**, *5*, 344–359.
189. Hao L, Huang H, Zhang Y, Ma T. Oxygen Vacant Semiconductor Photocatalysts. *Adv. Funct. Mater.* **2021**, *31*, 2100919.
190. Wang X, Ruan Y, Feng S, Chen S, Su K. Ag Clusters Anchored Conducting Polyaniline As Highly Efficient Cocatalyst for Cu_2ZnSnS_4 Nanocrystals toward Enhanced Photocatalytic Hydrogen Generation. *ACS Sustain. Chem. Eng.* **2018**, *6*, 11424–11432.
191. Liu XY, Chen H, Wang R, Shang Y, Zhang Q, Li W, et al. 0D-2D Quantum Dot: Metal Dichalcogenide Nanocomposite Photocatalyst Achieves Efficient Hydrogen Generation. *Adv. Mater.* **2017**, *29*, 1605646.
192. Chen Q, Liu Y, Gu X, Li D, Zhang D, Zhang D, et al. Carbon dots mediated charge sinking effect for boosting hydrogen evolution in Cu-In-Zn-S QDs/MoS_2 photocatalysts. *Appl. Catal. B* **2022**, *301*, 120755.
193. Wang L, Wang W, Sun S. A simple template-free synthesis of ultrathin Cu_2ZnSnS_4 nanosheets for highly stable photocatalytic H_2 evolution. *J. Mater. Chem.* **2012**, *22*, 6553.
194. Pan L, Dai L, Burton OJ, Chen L, Andrei V, Zhang Y, et al. High carrier mobility along the [111] orientation in Cu_2O photoelectrodes. *Nature* **2024**, *628*, 765–770.
195. Teitsworth TS, Hill DJ, Litvin SR, Ritchie ET, Park J-S, Custer JP, et al. Water splitting with silicon p–i–n superlattices suspended in solution. *Nature* **2023**, *614*, 270–274.
196. Tan J, Kang B, Kim K, Kang D, Lee H, Ma S, et al. Hydrogel protection strategy to stabilize water-splitting photoelectrodes. *Nat. Energy* **2022**, *7*, 537–547.
197. Jun SE, Kim Y-H, Kim J, Cheon WS, Choi S, Yang J, et al. Atomically dispersed iridium catalysts on silicon photoanode for efficient photoelectrochemical water splitting. *Nat. Commun.* **2023**, *14*, 609.
198. Yu Y, Zhang Z, Yin X, Kvit A, Liao Q, Kang Z, et al. Enhanced photoelectrochemical efficiency and stability using a conformal TiO_2 film on a black silicon photoanode. *Nat. Energy* **2017**, *2*, 17045.
199. Zhang JH, Zhang M, Dong YY, Bai CC, Feng YQ, Jiao L, et al. CdTe/CdSe-sensitized photocathode coupling with Ni-substituted polyoxometalate catalyst for photoelectrochemical generation of hydrogen. *Nano Res.* **2022**, *15*, 1347–1354.
200. Guo P, Xiao Y, Mo R, Li X, Li H. Coherent-Twinning-Enhanced Solar Water Splitting in Thin-Film Cu_2ZnSnS_4 Photocathodes. *ACS Energy Lett.* **2023**, *8*, 494–501.
201. Guijarro N, Lana-Villarreal T, Gomez R. Modulating the n- and p-type photoelectrochemical behavior of zinc copper indium sulfide quantum dots by an electrochemical treatment. *Chem. Commun.* **2012**, *48*, 7681–7683.
202. Liu Y, Xia M, Ren D, Nussbaum S, Yum J-H, Grätzel M, et al. Photoelectrochemical CO_2 Reduction at a Direct $CuInGaS_2$/Electrolyte Junction. *ACS Energy Lett.* **2023**, *8*, 1645–1651.
203. Ge J, Roland PJ, Koirala P, Meng W, Young JL, Petersen R, et al. Employing Overlayers To Improve the Performance of Cu_2BaSnS_4 Thin Film based Photoelectrochemical Water Reduction Devices. *Chem. Mater.* **2017**, *29*, 916–920.
204. Sun J, Guijarro N, Li P, Thumu U, Yum J-H, Sivula K, et al. Ink-Based $CuIn_{0.3}Ga_{0.7}S_2$ Nanocrystal Thin Films as Photocathodes for Photoelectrochemical CO_2 Reduction Reaction. *ACS Appl. Nano Mater.* **2023**, *6*, 10106–10114.
205. Chen Y, Chuang C-H, Lin K-C, Shen S, McCleese C, Guo L, et al. Synthesis and Photoelectrochemical Properties of $(Cu_2Sn)_xZn_{3(1-x)}S_3$ Nanocrystal Films. *J. Phys. Chem. C* **2014**, *118*, 11954–11963.
206. Nishi H, Kuwabata S, Torimoto T. Composition-Dependent Photoelectrochemical Properties of Nonstoichiometric Cu_2ZnSnS_4Nanoparticles. *J. Phys. Chem. C* **2013**, *117*, 21055–21063.
207. Guijarro N, Prevot MS, Sivula K. Enhancing the Charge Separation in Nanocrystalline Cu_2ZnSnS_4 Photocathodes for Photoelectrochemical Application: The Role of Surface Modifications. *J. Phys. Chem. Lett.* **2014**, *5*, 3902–3908.
208. Kato T, Hakari Y, Ikeda S, Jia Q, Iwase A, Kudo A. Utilization of Metal Sulfide Material of $(CuGa)_{1-x}Zn_{2x}S_2$ Solid Solution with Visible Light Response in Photocatalytic and Photoelectrochemical Solar Water Splitting Systems. *J. Phys. Chem. Lett.* **2015**, *6*, 1042–1047.

209. Hu Y, Pan Y, Wang Z, Lin T, Gao Y, Luo B, et al. Lattice distortion induced internal electric field in TiO_2 photoelectrode for efficient charge separation and transfer. *Nat. Commun.* **2020**, *11*, 2129.
210. Kang Z, Si H, Zhang S, Wu J, Sun Y, Liao Q, et al. Interface Engineering for Modulation of Charge Carrier Behavior in ZnO Photoelectrochemical Water Splitting. *Adv. Funct. Mater.* **2019**, *29*, 1808032.
211. Channa AI, Tong X, Xu J-Y, Liu Y, Wang C, Sial MN, et al. Tailored near-infrared-emitting colloidal heterostructured quantum dots with enhanced visible light absorption for high performance photoelectrochemical cells. *J. Mater. Chem. A* **2019**, *7*, 10225–10230.
212. Liu C, Tong X, Channa AI, Li X, Long Z, Feng H, et al. Tuning the composition of heavy metal-free quaternary quantum dots for improved photoelectrochemical performance. *J. Mater. Chem. A* **2021**, *9*, 5825–5832.
213. Xu J, Hu Z, Zhang J, Xiong W, Sun L, Wan L, et al. Cu_2ZnSnS_4 and $Cu_2ZnSn(S_{1-x}Se_x)_4$ nanocrystals: Room-temperature synthesis and efficient photoelectrochemical water splitting. *J. Mater. Chem. A* **2017**, *5*, 25230–25236.
214. Wu L. Cu-based mutlinary sulfide nanomaterials for photocatalytic applications. *AIMS Mater. Sci.* **2023**, *10*, 909–933.
215. Suryawanshi MP, Shin S-W, Ghorpade UV, Song D, Hong CW, Han S-S, et al. A Facile and Green Synthesis of Colloidal Cu_2ZnSnS_4 Nanocrystals and Their Application in High Efficient Solar Water Splitting. *J. Mater. Chem. A* **2017**, *5*, 4695–4709.
216. Jiao X, Zheng K, Liang L, Li X, Sun Y, Xie Y. Fundamentals and challenges of ultrathin 2D photocatalysts in boosting CO_2 photoreduction. *Chem. Soc. Rev.* **2020**, *49*, 6592–6604.
217. Wan L, Zhou Q, Wang X, Wood TE, Wang L, Duchesne PN, et al. Cu_2O nanocubes with mixed oxidation-state facets for (photo)catalytic hydrogenation of carbon dioxide. *Nat. Catal.* **2019**, *2*, 889–898.
218. Zhou B, Ma Y, Ou P, Ye Z, Li X-Y, Vanka S, et al. Light-driven synthesis of C_2H_6 from CO_2 and H_2O on a bimetallic AuIr composite supported on InGaN nanowires. *Nat. Catal.* **2023**, *6*, 987–995.
219. Fang S, Rahaman M, Bharti J, Reisner E, Robert M, Ozin GA, et al. Photocatalytic CO_2 reduction. *Nat. Revi. Methods Primers* **2023**, *3*, 61.
220. Zhou M, Wang S, Yang P, Huang C, Wang X. Boron Carbon Nitride Semiconductors Decorated with CdS Nanoparticles for Photocatalytic Reduction of CO_2. *ACS Catal.* **2018**, *8*, 4928–4936.
221. Pang H, Meng X, Li P, Chang K, Zhou W, Wang X, et al. Cation Vacancy-Initiated CO_2 Photoreduction over ZnS for Efficient Formate Production. *ACS Energy Lett.* **2019**, *4*, 1387–1393.
222. Xu JQ, Ju ZY, Zhang W, Pan Y, Zhu JF, Mao JW, et al. Efficient Infrared-Light-Driven CO_2 Reduction Over Ultrathin Metallic Ni-doped CoS_2 Nanosheets. *Angew. Chem. Int. Ed.* **2021**, *60*, 8705–8709.
223. Yoshino S, Iwase A, Yamaguchi Y, Suzuki TM, Morikawa T, Kudo A. Photocatalytic CO_2 Reduction Using Water as an Electron Donor under Visible Light Irradiation by Z-Scheme and Photoelectrochemical Systems over $(CuGa)_{0.5}ZnS_2$ in the Presence of Basic Additives. *J. Am. Chem. Soc.* **2022**, *144*, 2323–2332.
224. Wang L, Zhang Z, Guan R, Wu D, Shi W, Yu L, et al. Synergistic CO_2 reduction and tetracycline degradation by CuInZnS-Ti3C2Tx in one photoredox cycle. *Nano Res.* **2022**, *15*, 8010–8018.
225. Kong Y, Li Y, Zhang Y, Lin W. Unveiling the Selectivity of CO_2 Reduction on Cu_2ZnSnS_4: The Effect of Exposed Termination. *J. Phys. Chem. C* **2021**, *125*, 24967–24973.
226. Yoshida T, Yamaguchi A, Umezawa N, Miyauchi M. Photocatalytic CO_2 Reduction Using a Pristine Cu_2ZnSnS_4 Film Electrode under Visible Light Irradiation. *J. Phys. Chem. C* **2018**, *122*, 21695–21702.
227. Zubair M, Razzaq A, Grimes CA, In S-I. Cu_2ZnSnS_4 (CZTS)-ZnO: A noble metal-free hybrid Z-scheme photocatalyst for enhanced solar-spectrum photocatalytic conversion of CO_2 to CH_4. *J. CO2 Util.* **2017**, *20*, 301–311.
228. Xie Z, Xu W, Fang F, Zhang K, Yu X, Chang K. Gel-assisted synthesis of CIZS for visible-light photocatalytic reduction reaction. *Chem. Eng. J.* **2022**, *429*, 132364.
229. Chai Y, Kong Y, Lin M, Lin W, Shen J, Long J, et al. Metal to non-metal sites of metallic sulfides switching products from CO to CH_4 for photocatalytic CO_2 reduction. *Nat. Commun.* **2023**, *14*, 6168.
230. Qi M-Y, Lin Q, Tang Z-R, Xu Y-J. Photoredox coupling of benzyl alcohol oxidation with CO_2 reduction over CdS/TiO_2 heterostructure under visible light irradiation. *Appl. Catal. B* **2022**, *307*, 121158.
231. Yuan T, Sun L, Wu Z, Wang R, Cai X, Lin W, et al. Mild and metal-free Birch-type hydrogenation of (hetero)arenes with boron carbonitride in water. *Nat. Catal.* **2022**, *5*, 1157–1168.
232. Zhang LL, Liu L, Pan ZY, Zhang R, Gao ZY, Wang GM, et al. Visible-light-driven non-oxidative dehydrogenation of alkanes at ambient conditions. *Nat. Energy* **2022**, *7*, 1042–1051.
233. Somekh M, Khenkin AM, Herman A, Neumann R. Selective Visible Light Aerobic Photocatalytic Oxygenation of Alkanes to the Corresponding Carbonyl Compounds. *ACS Catal.* **2019**, *9*, 8819–8824.
234. Wu Y, Yuan B, Li M, Zhang W-H, Liu Y, Li C. Well-defined BiOCl colloidal ultrathin nanosheets: Synthesis, characterization, and application in photocatalytic aerobic oxidation of secondary amines. *Chem. Sci.* **2015**, *6*, 1873–1878.
235. Zhou S, Sun K, Toe CY, Yin J, Huang J, Zeng Y, et al. Engineering a Kesterite-Based Photocathode for Photoelectrochemical Ammonia Synthesis from NO(x) Reduction. *Adv. Mater.* **2022**, *34*, e2201670.

236. Wang P, Minegishi T, Ma G, Takanabe K, Satou Y, Maekawa S, et al. Photoelectrochemical conversion of toluene to methylcyclohexane as an organic hydride by Cu_2ZnSnS_4-based photoelectrode assemblies. *J. Am. Chem. Soc.* **2012**, *134*, 2469–2472.
237. Bhattacharyya B, Simlandy AK, Chakraborty A, Rajasekar GP, Aetukuri NB, Mukherjee S, et al. Efficient Photosynthesis of Organics from Aqueous Bicarbonate Ions by Quantum Dots Using Visible Light. *ACS Energy Lett.* **2018**, *3*, 1508–1514.
238. Ming H, Bian X, Cheng J, Yang C, Hou Y, Ding K, et al. Carbon nitride with a tailored electronic structure toward peroxymonosulfate activation: A direct electron transfer mechanism for organic pollutant degradation. *Appl. Catal. B* **2024**, *341*, 123314.
239. Wang K, Zeng S, Li G, Dong Y, Wang Q, Zhang L, et al. Superoxide radical induced redox processes for simultaneous reduction of Cr (VI) and oxidation of ciprofloxacin in wastewater. *Appl. Catal. B* **2024**, *343*, 123565.
240. Zhang H, Wang Z, Zhang J, Dai K. Metal-sulfide-based heterojunction photocatalysts: Principles, impact, applications, and in-situ characterization. *Chin. J. Catal.* **2023**, *49*, 42–67.
241. Zhang H, Zhou C, Zeng H, Deng L, Shi Z. Can Cu_2ZnSnS_4 nanoparticles be used as heterogeneous catalysts for sulfadiazine degradation? *J. Hazard. Mater.* **2020**, *395*, 122613.
242. Yang Y, Que W, Zhang X, Yin X, Xing Y, Que M, et al. High-quality Cu_2ZnSnS_4 and $Cu_2ZnSnSe_4$ nanocrystals hybrid with ZnO and $NaYF_4$: Yb, Tm as efficient photocatalytic sensitizers. *Appl. Catal. B* **2017**, *200*, 402–411.
243. Chen M-M, Xue H-G, Guo S-P. Multinary metal chalcogenides with tetrahedral structures for second-order nonlinear optical, photocatalytic, and photovoltaic applications. *Coord. Chem. Rev.* **2018**, *368*, 115–133.
244. Fan C-M, Regulacio MD, Ye C, Lim SH, Lua SK, Xu Q-H, et al. Colloidal nanocrystals of orthorhombic Cu_2ZnGeS_4: Phase-controlled synthesis, formation mechanism and photocatalytic behavior. *Nanoscale* **2015**, *7*, 3247–3253.
245. Semalti P, Sharma V, Sharma SN. A novel method of water remediation of organic pollutants and industrial wastes by solution-route processed CZTS nanocrystals. *J. Mater.* **2021**, *7*, 904–919.
246. Kush P, Deori K, Kumar A, Deka S. Efficient hydrogen/oxygen evolution and photocatalytic dye degradation and reduction of aqueous Cr(vi) by surfactant free hydrophilic Cu_2ZnSnS_4 nanoparticles. *J. Mater. Chem. A* **2015**, *3*, 8098–8106.
247. Dalui A, Thupakula U, Khan AH, Ghosh T, Satpati B, Acharya S. Mechanism of Versatile Catalytic Activities of Quaternary CuZnFeS Nanocrystals Designed by a Rapid Synthesis Route. *Small* **2015**, *11*, 1829–1839.